Journal of Geochemical Exploration 264 (2024) 107530

Contents lists available at ScienceDirect

Journal of Geochemical Exploration

journal homepage: www.elsevier.com/locate/gexplo

Cassiterite trace element discrimination diagrams to facilitate critical mineral exploration

Avish A. Kumar *, Ioan V. Sanislav, Huiqing Huang, Paul H.G.M. Dirks

Economic Geology Research Centre (EGRU), College of Science and Engineering, James Cook University, Townsville, Australia

ARTICLE INFO

Keywords:
Cassiterite
Critical metals
Scikit-learn
Cluster analysis
Discrimination diagram

ABSTRACT

Cassiterite is a weathering-resistant mineral, which can incorporate a variety of trace elements. Trace elements in cassiterite samples collected from twelve deposits in the Herberton Mineral Field, Australia, were measured with the use of laser ablation inductively coupled plasma mass spectrometry (LA-ICP-MS). The results were combined with published data from other tin fields, including the Andean Sn belt in South America; the Karagwe Ankole belt in Rwanda; and, from China, the Kangxiwa-Dahongliutan pegmatite field, the Youjiang basin, the Nanling belt and the Da Hinggan Range belt. Tin deposits in the dataset can be subdivided into four deposit types: 1) greisen and veins; 2) skarns; 3) Li-Cs-Ta pegmatites; and 4) polymetallic veins. The cassiterite dataset was analyzed using basic descriptive statistics, principal component analysis (PCA), and cluster analysis. Cassiterite grains from greisen and vein deposits are characterized by high concentrations of Ti (avg. 1751 ppm) and moderate concentrations of Al (avg. 97 ppm), whereas cassiterite grains from skarn deposits generally contain lower concentrations of Ti and Al. Chemical compositional boundaries in cassiterite from different deposits were recognized with cluster analysis. The relative enrichment of Al and Ti in cassiterite grains from greisen and vein deposits is likely due to greisenization reactions. The Ti vs. Al diagram can be used to differentiate between cassiterite grains derived from greisen and vein deposits, as compared to cassiterite grains derived from skarn deposits, whereas Sb vs. V diagram can be used to differentiate between cassiterite grains from polymetallic vein deposits. Zirconium and Nb concentrations are useful in identifying cassiterite grains sourced from LCT pegmatite deposits. The discrimination diagrams developed in this study through cluster analysis indicate that cassiterite grains sourced from different deposit types can be differentiated based on their trace element geochemistry and this can be a useful tool in critical mineral exploration. Therefore, these diagrams can be used effectively to understand metal association and deposit types in a region with detrital cassiterite from stream sediments, till and heavy mineral placer deposits.

1. Introduction

Cassiterite is a weathering resistant, chemically inert, heavy mineral which can accumulate in stream sediments (Aleva, 1985; Konopelko et al., 2022; Nwamba et al., 2023). This makes cassiterite a useful indicator mineral that can be used in exploration of different deposit types. Cassiterite-bearing greisen, quartz-vein, skarn, and polymetallic deposits are of hydrothermal origin (Tindle and Breaks, 1998; Kendall-Langley et al., 2020), whereas pegmatite deposits have a magmatic origin (London, 2018). Concentrations of Fe, Mn, Nb, and Ta in cassiterite have been used to differentiate between hydrothermal- and pegmatite-related cassiterite deposits (Tindle and Breaks, 1998; Bennett et al., 2024). However, compositional variations between cassiterite grains originating from different hydrothermal tin deposits are not well understood.

Wang et al. (2022) added some clarity to the differences observed in cassiterite trace elements geochemistry from different deposit types. Their research suggests that Sc vs. V, Sc vs. Ta, and Sc vs. Nb plots could fingerprint cassiterite from different deposits (Wang et al., 2022). Our research further improves this understanding by proposing discrimination plots and interpretations for the cycling of metals in deposits and the substitution of elements in cassiterite observed in different hydrothermal tin deposits. Tin fields that host these cassiterite-bearing deposits display well-developed metal zonation for Li, Sn, W, Mo, Cu, Zn, Pb, and Ag (Taylor and Cuff, 1979; Lehmann, 1990; Audétat et al., 2000; Černý et al., 2005; London, 2014; Kumar et al., 2023a). A discrimination

* Corresponding author at: Room 160, Building 34, College of Science & Engineering, James Cook University, James Cook Drive, Douglas, Townsville, Australia.
E-mail address: avish.kumar@jcu.edu.au (A.A. Kumar).

https://doi.org/10.1016/j.gexplo.2024.107530
Received 26 October 2023; Received in revised form 12 May 2024; Accepted 16 June 2024
Available online 21 June 2024

plot for metal associated with the cassiterite-bearing deposits, including Li, Cu, and Zn, was also developed in this research.

Element substitutions and chemical differentiation recorded in cassiterite are generally related to the composition and physicochemical conditions of the mineralizing fluids (Izoret et al., 1985; Dusausoy et al., 1988; Möller et al., 1988; Neiva, 1996, 2008; Masau et al., 2000; Maldener et al., 2001; Pal et al., 2007). The composition and physicochemical character of the hydrothermal fluids are likely different between deposit types, which may be reflected in the geochemistry of cassiterite. Certain tetravalent elements including Ti, Zr, Hf, W, and U can substitute for Sn directly (Cheng et al., 2019), whereas other elements participate in coupled substitution reactions (Wang et al., 2022).

In this study we compiled a trace element geochemical dataset for cassiterite grains collected from different deposit types around the world. This dataset has been combined with new compositional data obtained for cassiterite grains from mineral deposits in the Herberton Mineral Field (HMF) in Northeast Queensland. The compositional data include trace element concentrations analyzed with laser ablation-inductively coupled plasma-mass spectroscopy (LA-ICP-MS) for cassiterite grains from seven different tin belts that host four major tin deposit types including: 1) greisen and vein deposits; 2) skarns; 3) Li-Cs-Ta (LCT) pegmatites; and 4) polymetallic veins. The dataset was investigated with principal component analysis (PCA) and density-based spatial clustering of applications with noise (DBSCAN). The clusters recognized through this technique were used to develop discrimination plots that differentiates cassiterite-bearing deposits.

2. Distribution and tectonic setting of cassiterite-bearing deposits

Major cassiterite-bearing deposits occur in a variety of tectonic settings including continental arcs, back-arc rifts, and intracontinental and post-collisional extensional settings (Romer and Kroner, 2016). Cassiterite-bearing deposits related to continental arcs (Fig. 1) formed during the Oligocene to Miocene in the Andean Sn belt in Bolivia and Peru (Sempere, 1995; Mlynarczyk and Williams-Jones, 2005; Fontboté, 2018; Gemmrich et al., 2021), and during the Carboniferous to Permian in the HMF in northeastern Australia (Cheng et al., 2018; Poblete et al., 2021; Kumar et al., 2022). The Triassic deposits in the Andean Sn belt (Sempere et al., 2002; Spikings et al., 2016) formed in a back-arc, rift-related setting (Fig. 1). Cassiterite-bearing deposits that formed during intracontinental extension (Fig. 1) in the Jurassic can be found in the Youjiang basin (Wang et al., 2013; Xu et al., 2015; Zhao et al., 2018; Shu et al., 2021) and the Nanling metallogenic belt in South China (Li et al., 2012; Wang et al., 2013; Mao et al., 2021; Shu et al., 2021), whereas Cretaceous examples occur in the Da Hinggan Range polymetallic belt in North China (Wu et al., 2011; Zhou et al., 2012). Cassiterite is also a common constituent of LCT pegmatite deposits that formed in post-collisional extensional settings, such as the Sn-rich pegmatite deposits of the Kangxiwa-Dahongliutan pegmatite field in China (Liu et al., 2015; Yan et al., 2018), and the Karagwe Ankole pegmatite belt in Rwanda (Dewaele et al., 2011; Nambaje et al., 2021).

2.1. Geology of major cassiterite-bearing deposits

2.1.1. Greisen and vein deposits

The concentration of trace elements in cassiterite grains from greisen and vein deposits in the Youjiang basin (He et al., 2022b, 2022a), the Nanling metallogenic belt (Chen et al., 2022) and the HMF (Fig. 2; Kumar et al., 2022) have been included in this study. Cassiterite from the Gejiu tin deposit in the Youjiang basin has been linked to the emplacement of Cretaceous granites (Cheng and Mao, 2010). Greisen mineralization in the Gejiu deposit is associated with the formation of muscovite, quartz, feldspar, chalcopyrite, pyrrhotite, cassiterite, and scheelite (He et al., 2022b). In the Nanling metallogenic belt (Fig. 1), cassiterite deposits were linked to hydrothermal processes, which deposited cassiterite in veins during the intrusion of Jurassic granites (Zhao et al., 2005). These veins have a strike length of <1.8 km, and they contain muscovite, tourmaline, fluorite, sericite, cassiterite, arsenopyrite, pyrite and minor chalcopyrite (Chen et al., 2022). In the HMF, greisen ores occur in the apical portions of fractionated Carboniferous granites (Kumar et al., 2022). Greisen ores are characterized by chlorite alteration in most of the HMF deposits (Clarke and Chang, 2017). This alteration may have resulted from the same hydrothermal activity that formed Cu- and Zn-sulfide deposits (Kumar et al., 2022, 2023b, 2023a).

2.1.2. Skarn deposits

Tin skarn deposits with cassiterite are associated with silica-rich (>

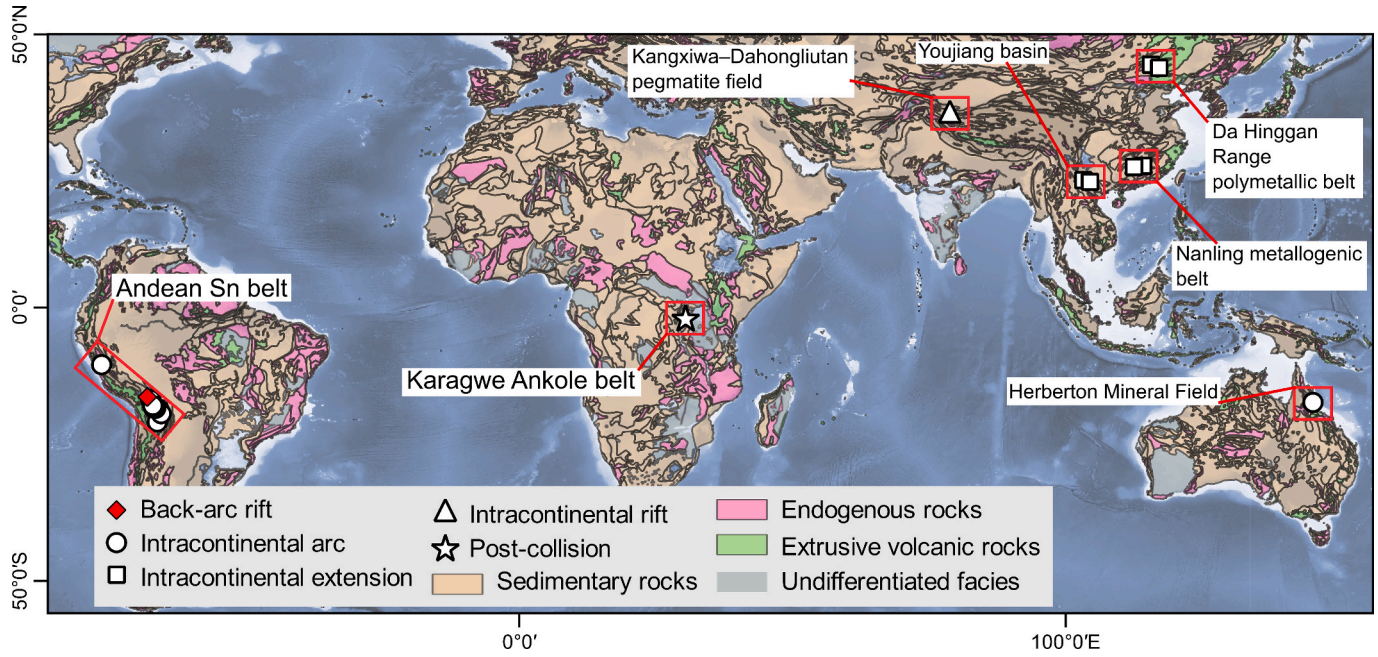

Fig. 1. Simplified map showing global distribution of tin fields included in this study. This map was generated from GIS data available through OneGeology (onegeology.org).

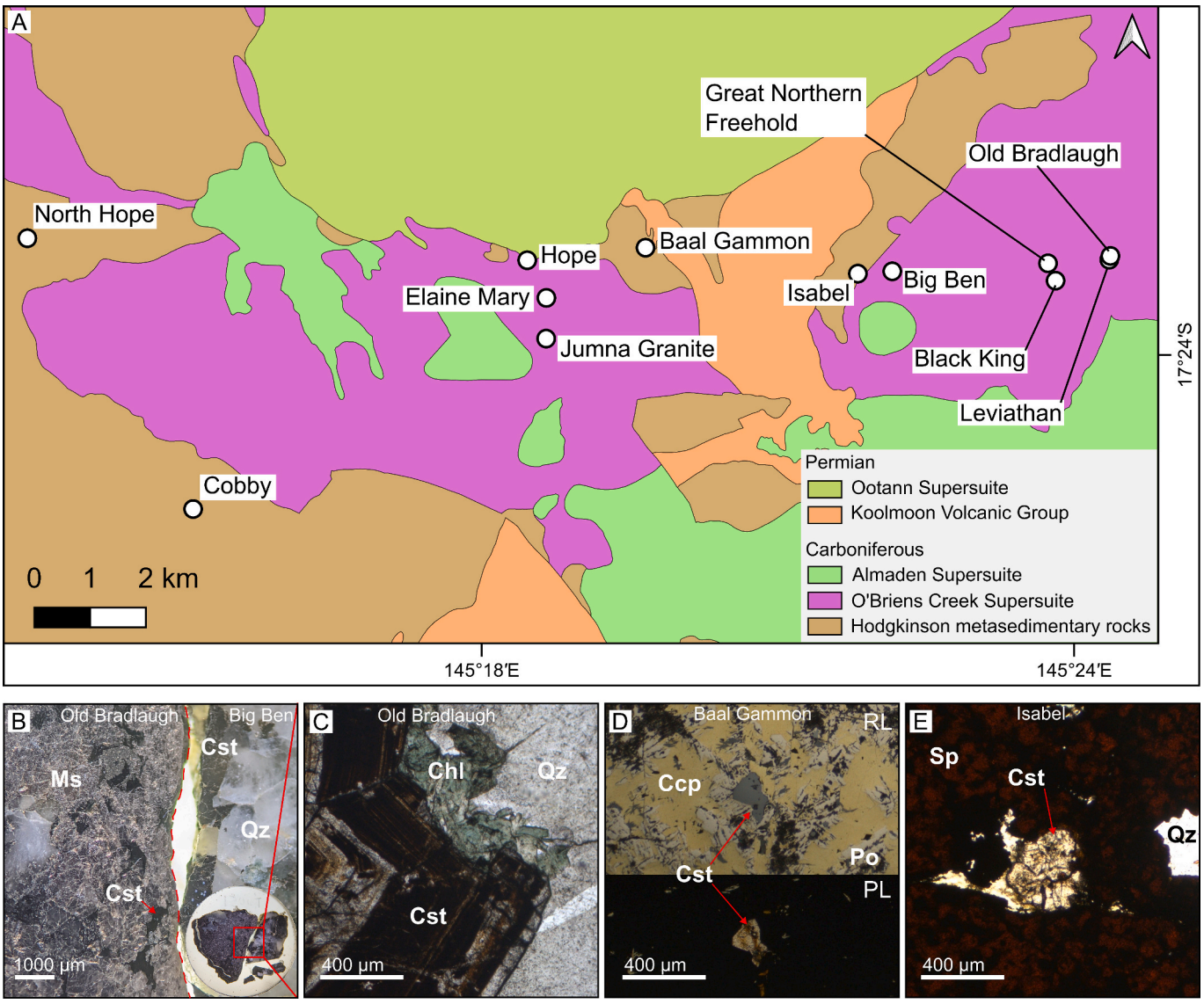

Fig. 2. A) Simplified geological map of the Herberton Mineral Field, and cassiterite photomicrographs of: B) Old Bradlaugh and Big Ben greisen and vein deposits showing cassiterite (Cst) in muscovite (Ms) and quartz (Qz), C) Old Bradlaugh sample showing cassiterite associated with chlorite alteration, D) Baal Gammon sample showing cassiterite in chalcopyrite (Ccp) and pyrrhotite (Po) in both reflected (RL) and plane polarized (PL) light, E) Isabel sample showing cassiterite in sphalerite (Sp).

70 % SiO_2) fractionated intrusions (Meinert, 1992). Like most skarns, tin systems are mineralogically zoned, with garnet, pyroxene, epidote and calcite occurring proximal to high-grade zones, whilst sulfide minerals are more common in the distal zones (Layne and Spooner, 1991; Meinert, 1992; Halley and Walshe, 1995). Cassiterite trace element data from tin skarn deposits were compiled for the Nanling metallogenic belt (Fig. 1; Chen et al., 2022), the Youjian basin (Fig. 1; He et al., 2022b, 2022a), the Da Hinggan Range polymetallic belt (Fig. 1; Li et al., 2022a), and the Andean tin belt (Fig. 1; Benites et al., 2022). The Furong Sn deposit in the Nanling metallogenic belt is associated with multi-phased Jurassic granite emplacement of A-type affinity and is enriched in W (Fig. 2B; Mao et al., 2013; Li et al., 2018; Yuan et al., 2019). Cassiterite in the Furong deposit formed during the retrograde skarn stage together with vesuvianite, pargasite, phlogopite, and magnetite (Chen et al., 2022). In the Gejiu deposit in the Youjian basin (Fig. 1), tin skarn deposits are concentrated along the contact zones of porphyritic granite and carbonate rocks (Chen et al., 1992, 2022). The Gejiu deposit also contains Cu sulfides associated with the retrograde skarn assemblages (Chen et al., 1992, 2022). The Ayawilca deposit in the Andean tin belt (Fig. 1), where the retrograde skarn stage was overprinted by sulfide and cassiterite, displays a similar mineralogy to the Gejiu deposit, but it also contains a significant quantity of sulfosalts (Benites et al., 2022). The deposit occurs as replacement veins hosted in Triassic-Jurassic carbonates (Benites et al., 2022). At the Huanggangliang deposit in the Da Hinggan Range polymetallic belt (Fig. 1), cassiterite together with other retrograde minerals including magnetite, scheelite, and sulfides, replace garnet and diopside that had formed earlier during a prograde skarn stage (Li et al., 2022a). Tin skarn deposits usually contain greisen alterations in the high-silica intrusions (Meinert, 1992; Mao et al., 1996).

2.1.3. *LCT pegmatite deposits*

Cassiterite is common in LCT pegmatites and occurs in the outer zones with albite-lepidolite bodies (London, 2014, 2018; Dill, 2015; Steiner, 2019). LCT pegmatites generally form in two possible ways: 1). via fractionation of tin-bearing, S-type granites; or 2). through crystallization of the partial melts of country rocks (Selway et al., 2005; Simmons et al., 2016; Konzett et al., 2018). Cassiterite trace element data has been compiled for LCT pegmatite deposits in the Kangxiwa-

Table 1
Summary of cassiterite sample locations and deposits included in this study.

Tin deposit type	Deposit location (n = number of cassiterite analysis)	Metal association	References
Greisen and vein	Jumna Granite, Herberton, Queensland, Australia (n = 22)	Sn	This study
	Big Ben, Herberton, Queensland, Australia (n = 19)	Sn	
	Black King, Herberton, Queensland, Australia (n = 23)	Sn	
	Brads Mine, Herberton, Queensland, Australia (n = 2)	Sn	
	Cobby, Herberton, Queensland, Australia (n = 18)	Sn	
	Elaine Mary, Herberton, Queensland, Australia (n = 28)	Sn	
	Great North Freeman, Herberton, Queensland, Australia (n = 14)	Sn	
	Hope Mine, Herberton, Queensland, Australia (n = 29)	Sn	
	Levianthan, Herberton, Queensland, Australia (n = 27)	Sn	
	North Hope Mine, Herberton, Queensland, Australia (n = 29)	Sn	
	Old Bradlaugh, Herberton, Queensland, Australia (n = 25)	Sn	
	Furong, Beihu district, China (n = 12)	Sn	Chen et al., 2022
	Gejiu, Yunnan Province, China (n = 122)	Sn	He et al., 2022b, 2022a
	Gatumba, Karagwe, Rwanda (n = 27)	Sn	Nambaje et al., 2020
	Rwinkwavu, Karagwe, Rwanda (n = 62)	Sn	
	Gisozi, Karagwe, Rwanda (n = 1)	Sn	
	Bigugu, Karagwe, Rwanda (n = 9)	Sn	
	Rwamagana, Karagwe, Rwanda (n = 4)	Sn	
	Rutongo, Karagwe, Rwanda (n = 5)	Sn	
Skarn	Ayawilca, Pasco, Peru (n = 17)	Sn, Zn	Benites et al., 2022
	Furong, Beihu district, China (n = 127)	Sn, W	Chen et al., 2022
	Gejiu, Yunnan Province, China (n = 65)	Sn	He et al., 2022b, 2022a
	Huanggangliang, Inner Mongolia, China (n = 38)	Sn, Fe	Li et al., 2022a
LCT pegmatite	Bigugu, Karagwe, Rwanda (n = 9)	Sn, Li, Nb, Ta	Nambaje et al., 2020
	Gatumba, Karagwe, Rwanda (n = 1)	Sn, Li, Nb, Ta	
	Rwinkwavu, Karagwe, Rwanda (n = 20)	Sn, Li, Nb, Ta	
	Ngara, Karagwe, Rwanda (n = 8)	Sn, Li, Nb, Ta	
Polymetallic vein	Baal Gammon, Herberton, Queensland, Australia (n = 17)	Sn, Cu	This study
	Isabel, Herberton, Queensland, Australia (n = 17)	Sn, Zn	
	Gejiu, Yunnan Province, China (n = 241)	Sn, Cu	He et al., 2022b, 2022a
	Ánimas-Chocaya-Siete Suyos, Potosi, Bolivia (n = 5)	Sn, Zn	Gemmrich et al., 2021
	Colquechaca, Potosi, Bolivia (n = 1)	Sn, Zn	
	Huanuni, Oruro, Bolivia (n = 58)	Sn, W, Zn	
	Huari Huari, Potosi, Bolivia (n = 5)	Sn, Zn	
	Kellhuani, La Paz, Bolivia (n = 29)	Sn, W, Zn	
	Llallagua, Potosi, Bolivia (n = 12)	Sn	
	San José-Itos, Oruro, Bolivia (n = 20)	Sn, Zn	
	Poopó, Oruro, Bolivia (n = 4)	Sn, Zn	
	Viloco, La Paz, Bolivia (n = 46)	Sn, W, Cu	

Dahongliutan pegmatite field (Fig. 1; Feng et al., 2019) and the Karagwe Ankole mineral belt (Fig. 1; Nambaje et al., 2020). The Kangxiwa-Dahongliutan pegmatites are genetically related to Triassic, calc-alkaline, S-type granites that are hosted in low-grade metasandstone (Yan et al., 2018; Feng et al., 2019). The orientation of emplacement of the pegmatite bodies was controlled by the strike direction of local faults (Feng et al., 2019). In the Karagwe Ankole belt, cassiterite occurs in quartz-mica veins of Neoproterozoic age LCT pegmatites (Nambaje et al., 2020). These pegmatite bodies have been linked to Neoproterozoic S-type granites that were emplaced after the amalgamation of Rodinia (Nambaje et al., 2021), while those in the Kangxiwa-Dahongliutan pegmatite field were linked to the Mazar-Kangxiwa suture zone on the Tibetan Plateau (Feng et al., 2019).

2.1.4. Polymetallic vein deposits

Cassiterite in polymetallic vein deposits occurs together with Cu, Zn, and Pb sulfides. Sulfides in tin deposits can be related to the Sn-bearing fluids (Kelly and Turneaure, 1970; Lehmann, 2021), or they can be sourced from a different fluid unrelated to Sn mineralization (Sillitoe and Lehmann, 2022). Trace element geochemistry of cassiterite that were compiled from polymetallic vein deposits in the Andean tin belt (Fig. 1; Gemmrich et al., 2021; Benites et al., 2022), the Youjiang basin (Fig. 1; He et al., 2022a) and the HMF (Figs. 1 and 2) have been included in this study. Other tin deposits, such as those in SW England (Andersen et al., 2016) and Tasmania (Denholm et al., 2021), also host significant sulfide mineralization. For the polymetallic Baal Gammon deposit in the HMF, chalcopyrite mineralization can be linked to the intrusion of oxidized Permian porphyries and granites (Kumar et al., 2022). The Andean Sn-Cu deposits generally occur in close spatial association with Oligocene-Miocene granites, and the Sn-Zn deposits are hosted in distal metasedimentary rocks (Cacho et al., 2019; Torró et al., 2019; Gemmrich et al., 2021). A similar style of metal zonation is also present in the Gejiu tin field where Sn-Cu enrichment occurs mostly along the contact of porphyritic granites, and Sn-Zn ± Pb ores were deposited along fracture zones in distal metasedimentary units (Cheng et al., 2013). The differences in metal zonation patterns in different mineral fields could be related to the local lithology. For example, the Gejiu and the Andean tin fields hosts skarn with greisen alteration in carbonaceous units (Cheng et al., 2013; Gemmrich et al., 2021), whereas the HMF mostly hosts greisen in metasandstones (Cheng et al., 2018).

3. Material and methods

3.1. Samples

Trace element data for cassiterite was compiled by combining new analyses from the HMF with published analyses from other tin fields. Hierarchical selection of samples was conducted to analyze representative cassiterite grains from mineral paragenetic sequence from deposits in the HMF (Fig. 2) and literature. A summary of the cassiterite samples used in this study has been presented in Table 1. Tin deposits for which analyses were used in this study include the Furong, Gejiu, and Huanggangliang deposits in China; the Ánimas-Chocaya-Siete Suyos, Potosi, Colquechaca, Huanuni, Huari Huari, Kellhuani, Llallagua, San José-Itos, Poopó, and Viloco deposits in Bolivia; the Rwinkwavu, Gisozi, Bigugu, Rutongo, Rwamagana, and Ngara deposits in Rwanda; the

Ayawilca deposit in Peru; and the Big Ben, Black King, Brads Mine, Cobby, Elaine Mary, Great North Freeman, Hope Mine, Levianthan, North Hope Mine, Old Bradlaugh, Baal Gammon, Isabel, and Jumna Granite deposits in Australia (Table 1 and Appendix 1). Examples of cassiterite mineralization have been presented in Fig. 2. The cassiterite samples from the HMF that were used for LA-ICP-MS analyses, were obtained from the Roger Taylor collection at the Herberton Mining Museum and the Economic Geology Research Centre at James Cook University.

3.2. Analytical methods

In situ trace element analyses were conducted on cassiterite samples with the use of an Analyte G2 Excimer Laser Ablation System coupled to a Thermo iCap-TQ ICP-MS (LA-ICP-MS) instrument at the Advanced Analytical Centre, James Cook University, Australia. Laser ablation of cassiterite was carried out at an energy density of 3 J/cm^2, at a rate of 5 Hz and a spot size of 50 μm. Multiple standards were used: NIST610 was used as an internal standard; while GSE-1, GSD-1, and NIST612 were used for bracketing and as external standards to monitor matrix effects. All cassiterite trace element data collected from the literature was obtained by LA-ICP-MS analysis (Table 1 and Appendix 1). Contamination was avoided by analyzing inclusion free cassiterite surfaces and selecting smooth constant signal segments in time-resolved ablation spectra. The ablation spectra were reduced using Iolite 4 software (Paton et al., 2011; Huang et al., 2021). A summary of the dataset is presented in Table 2. The dataset contains 1218 cassiterite analyses (Table 1) consisting of 478 greisen and vein, 247 skarn, 38 LCT pegmatite, and 455 polymetallic vein deposit samples, and the elements included are Al, Sc, Ti, V, Fe, Co, Ga, Zr, Nb, and Sb (Table 2).

3.3. Statistical methods

Descriptive statistics, principal component analysis (PCA), and cluster analysis were used to identify natural trends and groupings in the cassiterite dataset, where values below the limit of detection were not included. Multielement correlation matrices were developed for each deposit type, and binary plots were created for elements with a correlation coefficient (r) > 0.5, except for polymetallic veins where $r > 0.4$ was used (Appendix 2). Generally, low r values were observed for polymetallic vein deposits. PCA was applied to identify difference in geochemical signatures for cassiterite trace element concentrations in different deposit types. PCA technique summarizes multivariate data and projects the variance as components in decreasing order (Izenman, 2013; Jansson et al., 2022). Since PCA is sensitive to anomalies in the dataset (Dmitrijeva et al., 2020; Ge et al., 2022; Jansson et al., 2022), the dataset was standardized using the standard scaler preprocessing method in Scikit-learn in Python (Pedregosa et al., 2011; Hao and Ho, 2019).

A common practice when developing statistical models from compositional data is the application of log transformation on the dataset (Frenzel, 2023). On a cartesian plane, log transformation eliminates radial distortion (Aitchison, 1982; Aitchison et al., 2000; Scealy and Welsh, 2014), and this introduces symmetry to the dataset (Verhaegen et al., 2019). Log transformations or a variant of lognormal compositional space does not separate cassiterite composition for related hydrothermal deposits (Appendix 3) and these hydrothermal deposits are interconnected and contain signatures of fluid mixing from end-member deposit types. Weltje (2012) mentioned that according to log-ratio theory, the compositional data and their mixtures, on a cartesian plane, exists in different 1D and 3D spaces, and they cannot be combined into a statistical model (Verhaegen et al., 2019). In contrast, the log-transformed PCA plots yield meaningful results for independent deposit types, such as LCT pegmatite and hydrothermal cassiterite-bearing deposits (Appendix 3), but this information can also be derived from the results of standard scaler preprocessing models. Therefore, in this study the standard scaler preprocessing was used to construct interpretable compositional space for cassiterite trace element dataset.

Principal components or dimensionality reduced axes with eigenvalues greater than one were used. The eigenvectors define the principal axes, while the eigenvalues are a measure of the spread in the data. PCA results can be easily visualized with biplots, where PCA scores of individual samples are plotted with the loadings of the variables as vectors.

Table 2
Descriptive statistics of cassiterite trace element data.

Deposit type	Statistics	Al	Sc	Ti	V	Fe	Co	Ga	Zr	Nb	Sb
Greisen and vein	Mean	97	130	1751	52	3969	13	7	77	372	17
(n = 478)	Std	190	268	1798	112	5114	3.70	9	101	636	25
	Min	0.20	0.09	0.90	0.09	55	3.10	0.04	0.10	0.05	0.18
	Max	2835	2066	11,870	808	26,267	19	51	595	4325	198
	Median	41	20	1465	16	1459	12	2.87	26	70	8
	25 % Quartile	14	3.21	315	4.98	559	10	0.81	3.98	9	2.00
	75 % Quartile	131	153	2457	40	6244	17	10	126	431	21
Skarn	Mean	55	35	318	28	3329	6	9	45	274	18
(n = 247)	Std	81	94	607	43	3440	2.86	14	76	649	24
	Min	0.20	0.10	1.10	0.02	166	1.33	0.10	0.05	0.01	0.30
	Max	470	727	5755	371	18,421	12	98	557	5150	127
	Median	210	1.10	260	0.25	3650	11	3.60	830	5700	0.73
	25 % Quartile	4.15	1.30	29	3.62	983	4.00	0.30	11	9	3.00
	75 % Quartile	74	19	326	34	4965	10	13	43	252	21
LCT pegmatite	Mean	326	1.23	424	1.05	3553	12	8	920	7094	0.78
(n = 38)	Std	299	0.63	404	1.93	2380	3.58	9	388	4274	0.26
	Min	22	0.38	10	0.01	73	9	0.54	135	1650	0.50
	Max	1020	2.40	1450	10	8100	30	32	1900	19,100	1.71
	Median	58	24.40	856	45	2130	10	4.37	34	24	20.70
	25 % Quartile	106	0.68	106	0.03	1405	9	2.4	658	4250	0.61
	75 % Quartile	420	1.66	673	1.13	5825	12	11	1158	8775	0.86
Polymetallic vein	Mean	330	56	1779	107	2958	8	45	58	155	132
(n = 455)	Std	1343	88	2361	233	2614	4.77	127	67	294	536
	Min	0.53	0.01	1.31	0.22	69.96	0.34	0.18	0.02	0.01	0.33
	Max	19,899	873	26,028	3938	18,000	64	1314	483	2008	5223
	Median	20	6	139	14	1790	4.50	2.10	26	71	7
	25 % Quartile	13	6	223	18	1052	4.95	1.76	5	2.05	8
	75 % Quartile	181	65	2662	110	4021	10	23	97	145	55

When eigenvectors are defined in PCA, the data points are transformed into scores. For our PCA, these variables are the trace elements measured in cassiterite, while the scores are the transformed concentration values of these elements.

DBSCAN was used to conduct cluster analysis on the cassiterite trace element data, with the use of Scikit-learn in Python (Jolly, 2018). DBSCAN groups element-element correlation data by identifying areas with high data density on a binary plot (Ester et al., 1996; Schubert et al., 2017). Two input parameters are required for DBSCAN, which are the minimum number of samples in a cluster and the maximum concentration difference between two points (Hong and Oh, 2021). The minimum number of samples in a cluster varied from 15 to 30, and the maximum concentration difference ranged from 0.02 to 0.2 for clustering. The clusters identified with Scikit-learn are assigned with labels represented by integers (Jolly, 2018). Three groups were recognized in the cassiterite trace elements data, and they were labelled as −1, 0, and 1. The DBSCAN method is known for its robustness, effectiveness in handling noise, and capability in identifying clusters of arbitrary shapes (Ester et al., 1996; Bäcklund et al., 2011; Schubert et al., 2017; Zhang et al., 2019).

4. Results

4.1. Trace elements in cassiterite

A summary of the average composition of cassiterite samples from different deposit types has been presented in Table 2. The most abundant trace element in cassiterite is Fe, with averages >2900 ppm (Table 2). Cassiterite grains from polymetallic vein deposits have the lowest Fe concentrations (avg. 2958 ppm), while cassiterite grains from greisen and vein deposits have the highest (avg. 3969 ppm). The cassiterite grains from the greisen and vein deposits also display a strong correlation between Fe and Ga (r = 0.75, Figs. 3 and 4). For skarn and LCT pegmatite deposit types, cassiterite grains display a strong correlation between Ga and Al (r = 0.85 for skarn, and r = 0.94 for LCT pegmatite; Fig. 3). This suggests that Ga is an important element in differentiating cassiterite samples from different deposit types.

Of the four deposit types, cassiterite grains from greisen and vein, and polymetallic vein deposits contain higher Ti concentrations when compared with cassiterite grains from skarn and LCT pegmatite deposits. The average concentration of Ti in cassiterite grains is 1751 ppm for greisen and vein deposits, 1779 ppm for polymetallic vein deposits, 318 ppm for skarn deposits, and 424 ppm for LCT pegmatite deposits. A moderately strong correlation was observed between Ti and Sc (r = 0.57) in cassiterite grains obtained from skarn deposits (Figs. 3 and 4). Cassiterite grains from LCT pegmatite deposits exhibit a moderately strong correlation between Ti and Sb (r = 0.62, Fig. 3). Therefore, these differences in Ti correlation with other elements across deposit types may indicate the usefulness of Ti in discriminating cassiterite from different Sn deposit types.

Cassiterite samples from polymetallic vein and LCT pegmatite deposits contain similar concentrations of Al, averaging 330 and 326 ppm, respectively. Cassiterite grains from the LCT pegmatite deposits show high Nb (avg. 7094 ppm) and Zr (avg. 920 ppm) concentrations (Table 2). Strong correlation is observed between Nb and Fe (r = 0.74), while Zr shows a strong correlation with Al (r = 0.78) and Ga (r = 0.75, Fig. 3). These differences in concentrations and correlation coefficients suggest that Nb and Zr may be useful in identifying cassiterite grains linked to LCT pegmatite deposits. The average concentrations of Sc, V, Co, Ga, and Sb are mostly below 150 ppm in cassiterite samples from all deposit types (Table 2). Cassiterite samples from polymetallic vein deposits generally do not exhibit any strong multielement correlations (Fig. 3), but a moderate correlation was observed between V and Sc (r = 0.50).

4.2. Classification of cassiterite trace elements data

Groupings in the cassiterite data were recognized with the use of PCA and DBSCAN. A summary of the PCA results is presented in Fig. 5. The eigenvalues of first four principal components are greater than one (Fig. 5A) and they account for 65 % of the variability in the cassiterite trace elements data (Fig. 5). The principal component 1 is characterized by positive loadings for V, Sc, Al, Fe, Sb, and Ga (Fig. 5). The loadings for V and Sc reflect the geochemistry of cassiterite samples from greisen and vein deposits, while Al, Fe, Sb, and Ga are linked to cassiterite samples from polymetallic vein deposits (Fig. 5B). Principal component 3 displays positive loadings for Co, Ti, V, and Sc, which is reflective of trace elements of cassiterite samples from greisen and vein deposits (Fig. 5C). Similar characteristics were observed for principal component 2. Principal component 2 further shows high positive loadings for Zr and Nb which is linked to cassiterite samples from LCT pegmatite deposits (Fig. 5B). Principal component 4 is characterized by positive loadings for Ti, V, Sb, and Ga. The loadings for Ga and Sb reflect the geochemistry of cassiterite samples from polymetallic vein deposits (Fig. 5D). The loadings for the four principal components generally indicate elements which are useful in discriminating cassiterite from different deposits.

The groupings recognized in cassiterite trace element data are presented in Fig. 6. Element pairs were used in DBSCAN to identify clusters in cassiterite trace element data. The element pair, Ti and Al, show groupings for cassiterite samples from greisen and vein (94 % in cluster −1) deposits (Fig. 6). Whereas cassiterite samples from greisen and vein, and skarn deposits form two major clusters (−1, and 0), and the boundary between these two clusters is useful in differentiating these two deposit types (Fig. 6). The element pair, V and Sb, show groupings for cassiterite from polymetallic vein (79 % in cluster −1) and LCT pegmatite (100 % in cluster 0) deposits (Fig. 6). No clear separation was observed between cassiterite samples from greisen and vein, and skarn deposits on V and Sb plot (Fig. 6). The boundary between LCT pegmatite and cassiterite from the remaining three deposit types is arbitrary (Fig. 6) and defined by Sb and V concentrations. Additionally, Nb and Zr element pair is useful in differentiating cassiterite samples linked to Cu, Zn and Li deposits occurring in Sn fields (Fig. 6). The element pair, Nb and Zr, shows grouping for cassiterite from Li deposits (95 % in cluster −1, Fig. 6). Cassiterite samples from Cu and Zn deposits mostly contain low Nb and Zr concentrations and they group separately (cluster 0, Fig. 6).

5. Discussion

5.1. Incorporation of trace elements in cassiterite in different deposit types

Multielement correlations (Fig. 3) and trends observed on binary plots (Fig. 4) can be used to make inferences on element substitution reactions in cassiterite (Fig. 7). Greisen and quartz vein deposits show a positive correlation between Ga and Fe. He et al. (2022b) proposed three possible coupled substitution reactions, including: Fe^{3+} and Ga^{5+} for 2 $(Sn, Ti)^{4+}$; Fe^{3+} and OH^{-} for Sn^{4+} and O^{2-}; and Fe^{3+} and H^{+} for Sn^{4+}. The Fe concentrations in cassiterite grains from greisen and vein deposits are higher than Ga, suggesting a higher ratio of Fe being substituted (Fig. 4). This may indicate a preference for the latter two substitution reactions in cassiterite. The OH^{-} and H^{+} ions required for these substitution reactions are likely available from fluids that caused greisenization of the host rocks (Witt, 1988; Halter et al., 1996). The high Fe (up to 26,000 ppm) concentrations in greisen and vein cassiterite grains are likely linked to the presence of micron-sized magnetite inclusions (Greaves et al., 1971).

Polymetallic vein cassiterite samples show a positive trend on V and Sc plot, which may indicate incorporation of these elements by coupled substitution (Fig. 4). Coupled substitution of $Sc^{3+}$and V^{5+} for 2 Sn^{4+} has been observed in cassiterite samples from skarn deposits (Wang et al., 2022). Our data suggests that these substitutions in cassiterite are likely

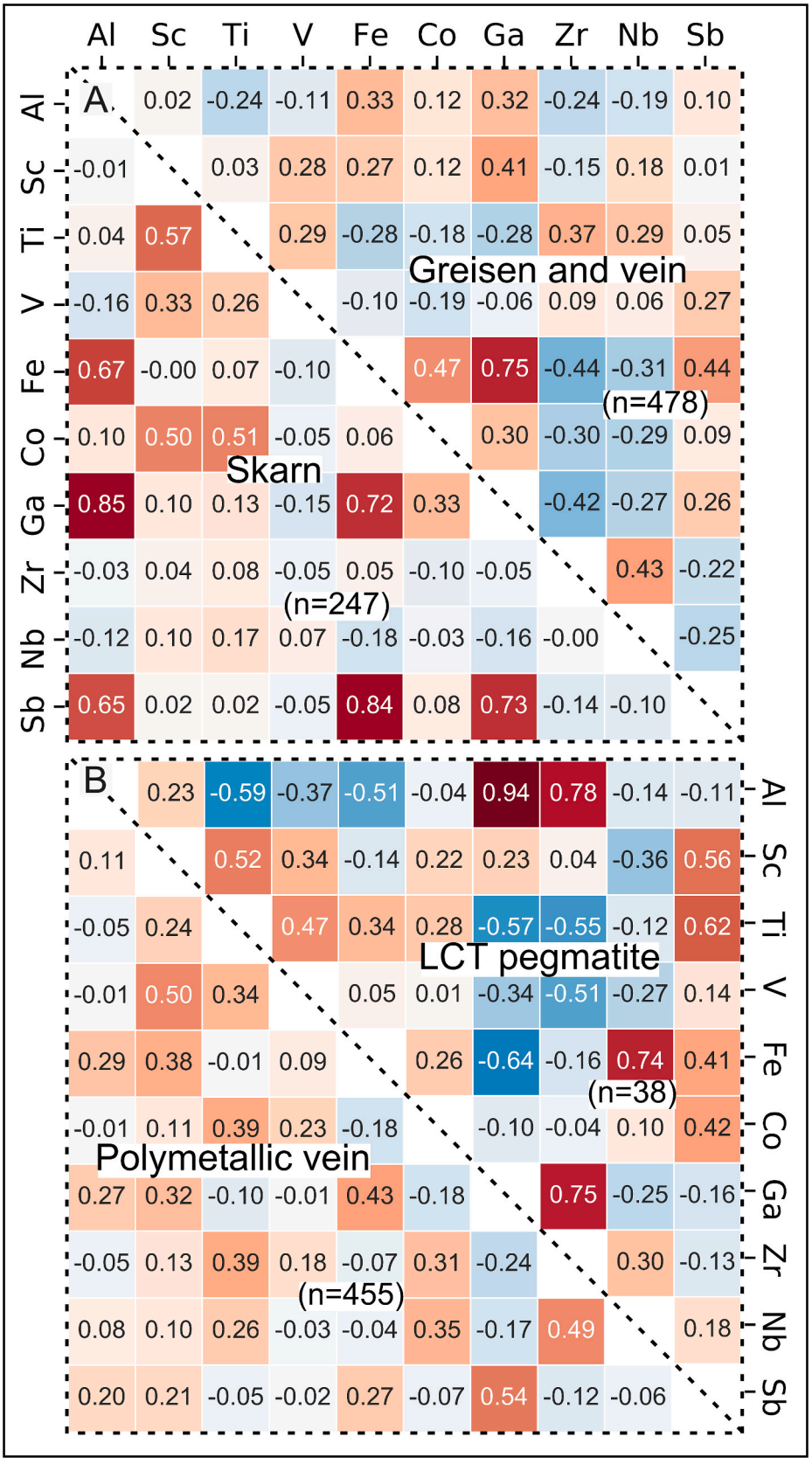

Fig. 3. Multielement correlations results of: A) greisen and vein, and skarn deposits, B) LCT pegmatite, and polymetallic vein deposits.

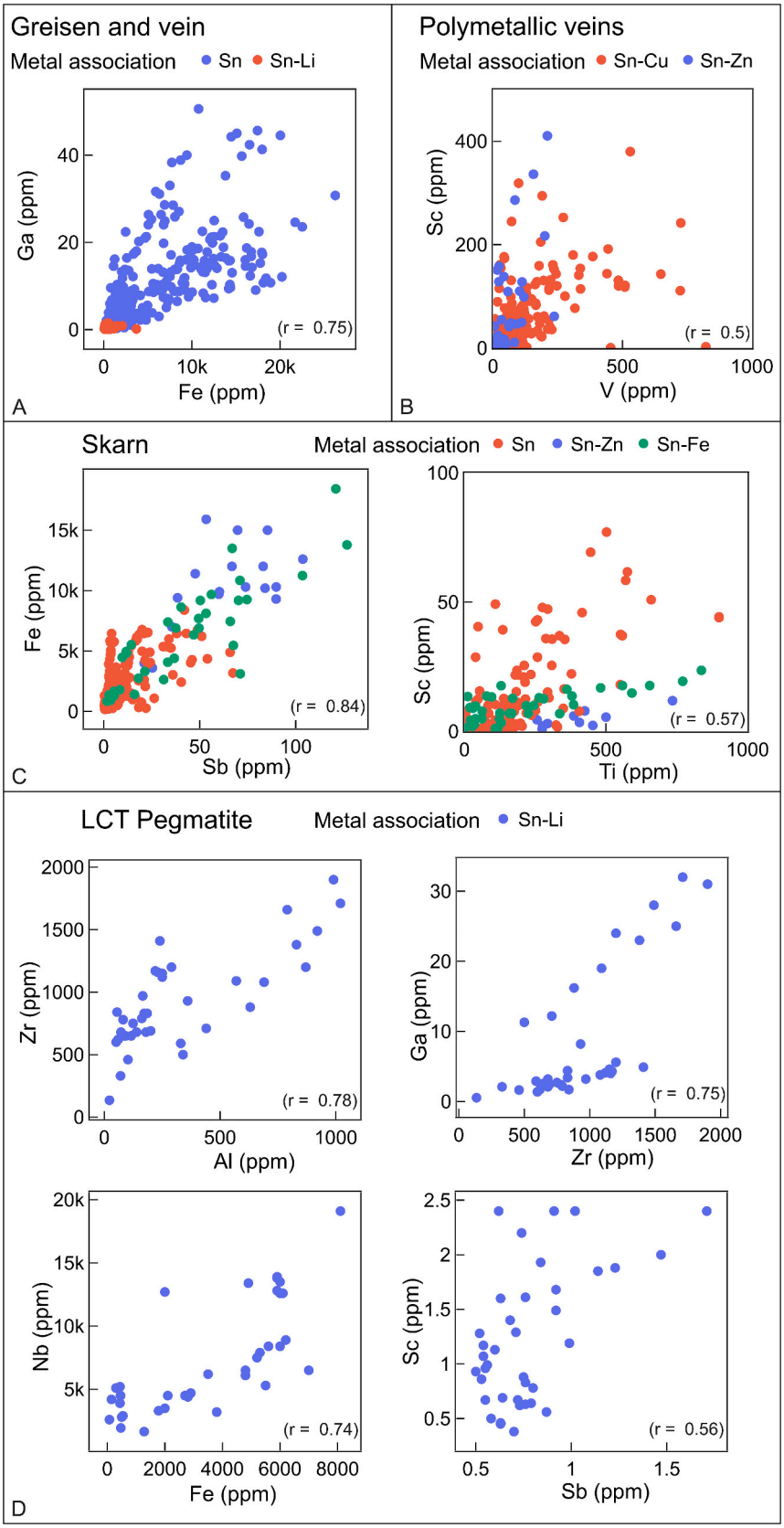

Fig. 4. Binary plots of selected trace elements from: A) greisen and vein, B) polymetallic vein, C) skarn, D) LCT pegmatite deposits.

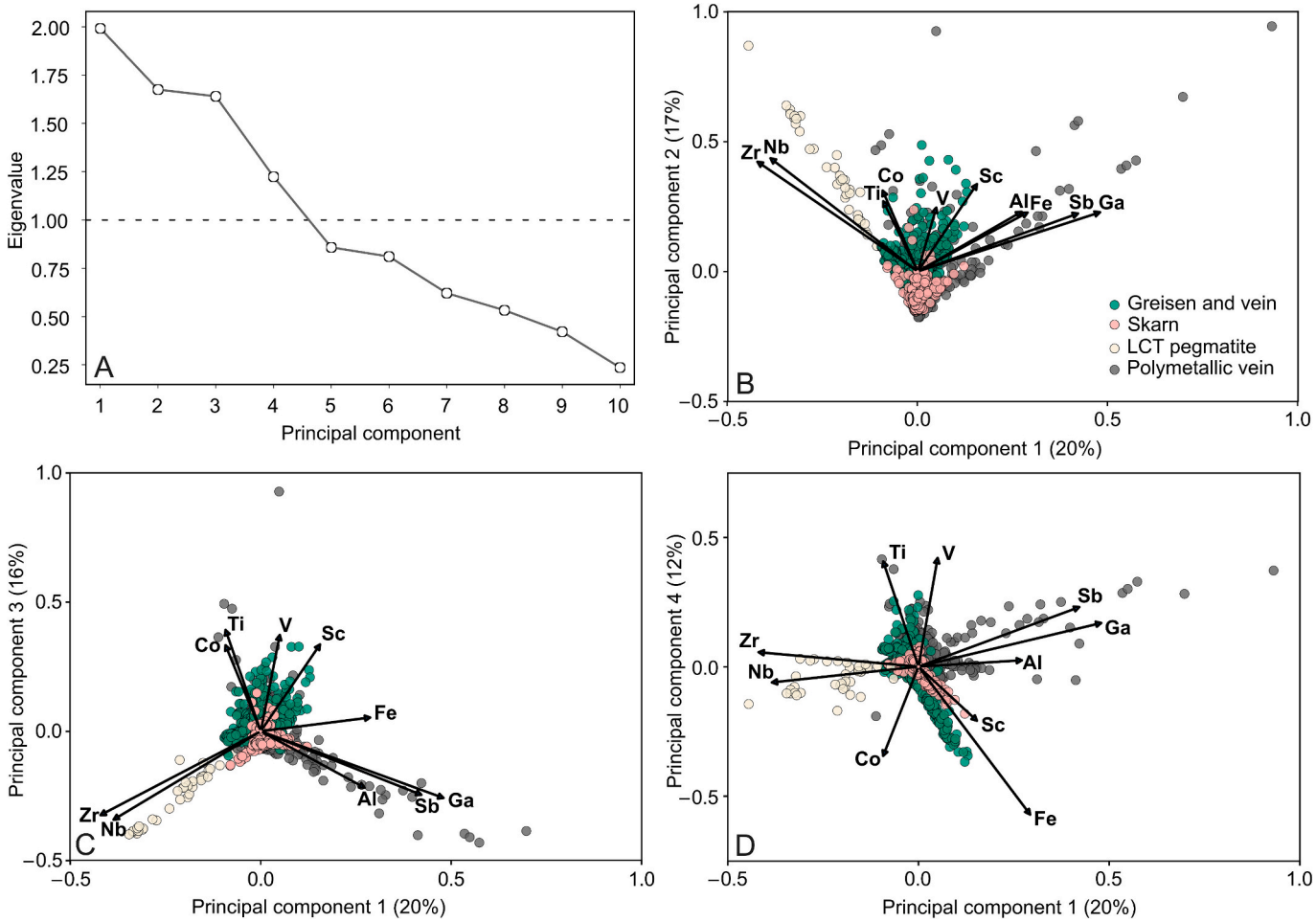

Fig. 5. Principal components analysis results showing: A) scree plot, B) score and loadings for principal component 1 and 2, C) score and loadings for principal component 1 and 3, and D) score and loadings for principal component 1 and 4.

favorable for Cu-rich polymetallic vein deposits (Fig. 4). Conversely, in cassiterite samples from Zn-rich polymetallic vein deposits, Ga^{5+} couples with Fe^{3+} to substitute for 2 Sn^{4+} (He et al., 2022b). Sphalerite is a common mineral in Zn-rich polymetallic vein deposits, and it contains significant amounts of Ga and Fe (Cook et al., 2009; Torró et al., 2022; Zhang et al., 2022). Therefore, Ga and Fe for the substitution reactions in cassiterite in Zn-rich polymetallic vein systems were likely derived from fluids that formed sphalerite.

Cassiterite samples from skarn deposits show a strong correlation between Sb and Fe ($r = 0.84$), and a moderately strong correlation between Sc and Ti ($r = 0.57$, Figs. 3 and 4). Cassiterite samples contain a higher concentration of Ti (avg. 318 ppm) compared to Sc (avg. 35 ppm), which may indicate a higher proportion of Ti had been substituted for Sn in cassiterite. This may have occurred through a direct substitution of Ti for Sn. Direct substitution of Ti^{4+} for Sn^{4+} in cassiterite grains has been observed in multiple studies (e.g., Cheng et al., 2019; Alekseev and Marin, 2022; Li et al., 2022b). Positive correlations were also observed between Fe and Ga ($r = 0.72$) in cassiterite samples from skarn deposits. Substitution of Fe and Ga for 2 Sn is a common characteristic of cassiterite grains linked to greisen deposits (He et al., 2022b). Cassiterite with strong correlation between Fe and Ga are likely associated with greisen alteration zones in skarn deposits. Greisen alteration in Sn skarn deposits is common (Meinert, 1992; Mao et al., 1996).

In LCT pegmatite deposits, cassiterite samples show a strong correlation between Zr and Al ($r = 0.78$, Fig. 3). Similarly strong correlations were also observed between Ga and Zr. The strong correlation and positive trend (Fig. 4) between Zr and Al and Ga and Zr may indicate element substitutions in LCT pegmatite cassiterite. Direct substitution of Zr^{4+} for Sn^{4+} was suggested by Cheng et al. (2019). Generally, Al (avg. 326 ppm) and Ga (avg. 8 ppm, Table 2) concentration in cassiterite is lower than Zr (avg. 920 ppm). The higher Zr concentrations measured in cassiterite may show preference for direct substitution of Zr by Sn. High concentrations of Nb (avg. 7094 ppm) are present in cassiterite samples from LCT pegmatite deposits. Hreus et al. (2021) suggested coupled substitution of $(Nb, Ta)^{5+}$ and $(Fe, Sc)^{3+}$ for 2 Sn^{4+} in cassiterite samples from Li-rich Sn deposits. A positive trend for Nb and Fe on the binary plot of cassiterite (Fig. 4), further confirms the presence of coupled substitution.

5.2. *Reliability of cassiterite discrimination diagrams*

Limitations identified during the design of this study were related to the lack of cassiterite trace element data from LCT pegmatite deposits and likely other deposit types (Table 1). Therefore, in this study a backbone for cassiterite discrimination diagrams is presented and this can be further improved by increasing the number of studied tin fields, cassiterite composition data, and elements used for discrimination analyses.

Due to the limitations of log-ratio transformation of compositional data on dependent variables and lower sample size, a scaler preprocessing method was used. To complement this, DBSCAN was used for clustering which handles noise effectively, but this may have introduced bias in the clusters. To improve these clusters, log-ratio or other variety of Box-Cox transformation (Atkinson et al., 2021; Frenzel, 2023; Olivier

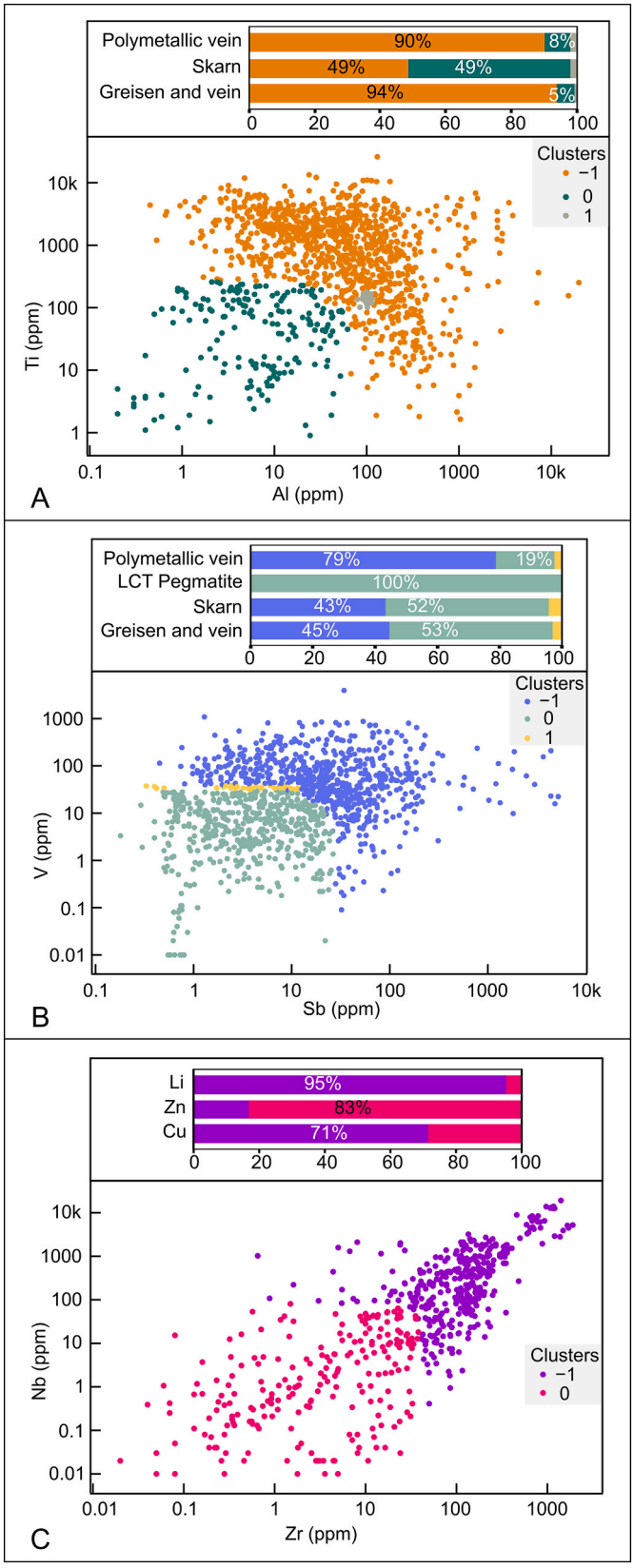

Fig. 6. DBSCAN and cluster statistics results for: A) Al vs. Ti, B) Sb vs. V, and C) Zr vs. Nb.

and Norberg, 2010) on larger sample size with Gaussian mixture model (Melnykov and Wang, 2023; Yang et al., 2012) is suggested for robust separation of dependent variables in a future study. Despite these limitations, the cassiterite discrimination diagrams were evaluated with data from Goldmann (2016) and accuracy >90 % for Al and Ti, > 80 % for Zr and Nb, and >55 % for Sb and V discrimination diagrams (Fig. 9) are observed.

5.3. Discrimination of cassiterite from different deposits

The cluster boundaries from DBSCAN (Fig. 6) results were used to develop discrimination plots (Fig. 8), which was supplemented with PCA (Fig. 5) and descriptive statistics (Table 2) results. These plots differentiate cassiterite from different deposits based on their trace element characteristics. Cassiterite samples from greisen and vein deposits are characterized by high Ti (avg. 1751 ppm) and moderate Al (avg. 97 ppm) concentrations (Table 2). In contrast, cassiterite samples from skarn deposits contain low concentrations of Ti (avg. 318 ppm) and Al (avg. 55 ppm, Table 2). The PCA results indicate that the loadings for Ti align with the scores for cassiterites from greisen and vein deposits on principal components 2 and 3 (Fig. 5). The Ti anomaly in cassiterite is likely linked to the fluids that generated fractionated granites and caused greisen alteration.

Greisen alteration is normally caused by hydrothermal processes active during the late stages of Sn granite evolution (Burt, 1981; Roberts, 2007; Launay et al., 2023). In tin granites, Ti is replaced by Sn in minerals, including titanite, magnetite, amphibole, and biotite (Meng et al., 2022; Niu et al., 2022), and this leads to a depletion in Ti (Lehmann, 2021). Micas and quartz from greisen assemblages contain Ti concentrations >100 ppm (Hreus et al., 2021; Breiter et al., 2023). This suggests that the hydrothermal fluids generated during the late stages of Sn granite evolution contain enough Ti for substitution with Sn in cassiterite. Alteration zones in skarn deposits have low Ti concentrations (Auwera and Andre, 1991; Abdelnasser et al., 2022), which is reflected in the cassiterite geochemistry. In greisen and vein deposits, Al is widely available during the greisenization process (Witt, 1988; Halter et al., 1996), but in skarn deposits it behaves as an immobile element (Abdelnasser et al., 2022). Therefore, cassiterite from greisen and vein, and skarn deposits can be differentiated by the chemical boundary shown on Al and Ti discrimination diagram (Fig. 8). This boundary was identified through DBSCAN, which was constructed from the grouping of cassiterites from greisen and vein (95 % of cassiterite), and skarn (49 % of cassiterite) deposits (Fig. 6). The greisen field of the Al and Ti discrimination plot was evaluated (Fig. 9) with cassiterite trace element data from Goldmann (2016) that was not included in the clustering dataset, and it shows that 92.6 % of the greisen cassiterite plot in the greisen field.

An overlapping field (33 % of cassiterite from skarn deposit) containing both greisen and skarn deposits was also identified on the Al and Ti discrimination plot (Fig. 8). The cassiterite samples from skarn deposits that plot in this overlapping field are likely linked to greisen alteration present in Sn skarn deposits (Meinert, 1992; Mao et al., 1996). The discrimination plot developed from Al and Ti (Fig. 8) shows compositional overlapping between cassiterite from greisen and vein, polymetallic vein, and LCT pegmatite deposits. This is likely due to fluids related to greisen and vein, and or skarn deposits causing polymetallic vein mineralization. In most Sn fields (Table 1), polymetallic vein deposits are closely associated with greisen or skarn deposits (e.g., Chen et al., 1992; Cheng et al., 2013; Gemmrich et al., 2021).

Cassiterite samples from polymetallic vein deposits can be differentiated by Sb and V discrimination plots (Figs. 6 and 8). This boundary was identified through DBSCAN, which was constructed from the groupings present in cassiterite from polymetallic vein (80 % of cassiterite), LCT pegmatite (80 % of cassiterite), skarn (52 % of cassiterite), and greisen and vein (53 % of cassiterite) deposits (Figs. 6 and 8). Cassiterite samples from polymetallic vein deposits are characterized by

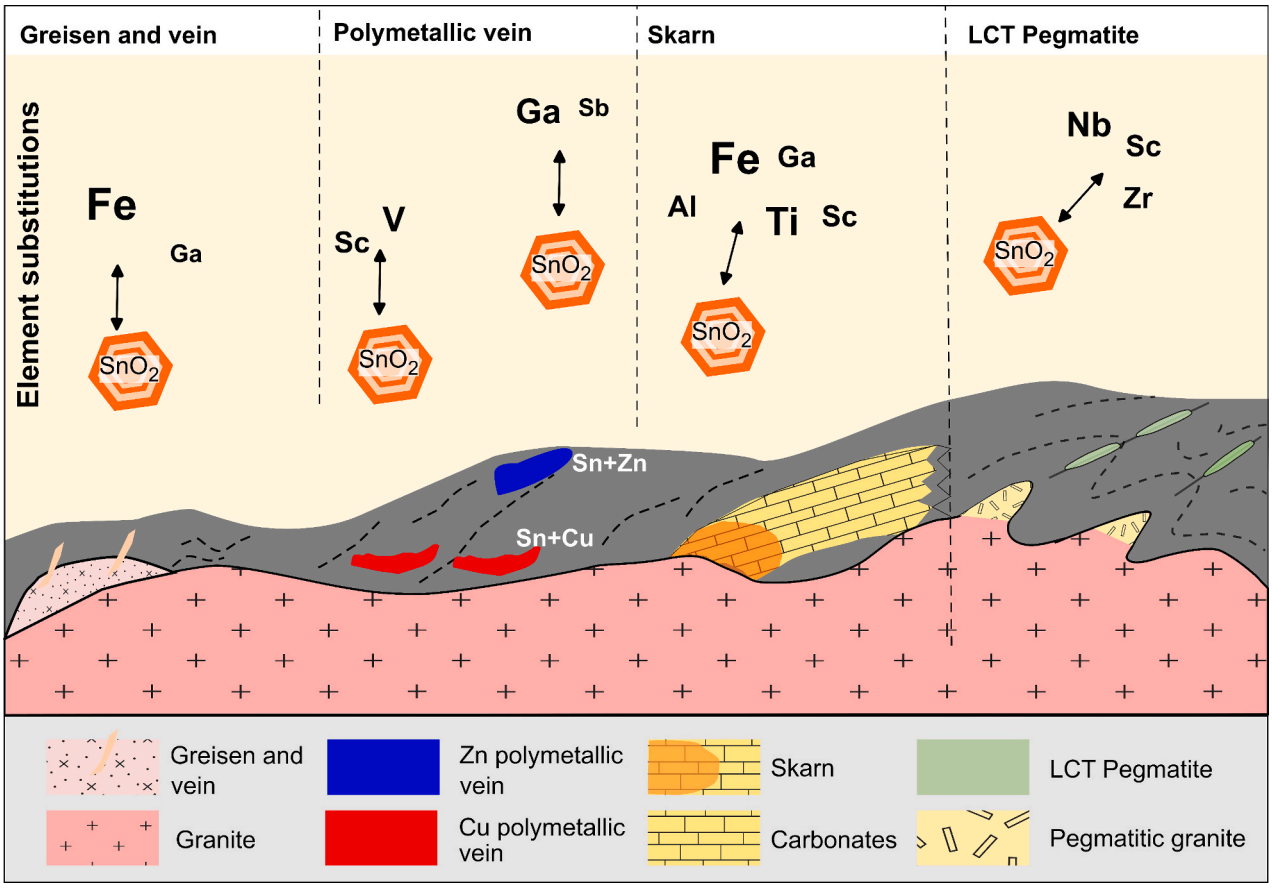

Fig. 7. Illustration of element substitutions in cassiterite from different deposit types. The element font size shows relative concentrations. The illustration was modified from Wang et al. (2022) and includes element substitutions mentioned in He et al. (2022b).

high concentrations of Sb (avg. 132 ppm) and V (avg. 107 ppm), which further supports this discrimination plot. The Sb and V discrimination plot was evaluated with cassiterite trace element data from Goldmann (2016) that was not included in the clustering dataset, and it shows that 58.3 % of the polymetallic vein cassiterite plot in the polymetallic field, and 53.2 % of the LCT pegmatite cassiterite plot in the LCT pegmatite field (Fig. 9). Cassiterite samples from greisen and skarn deposits show negative anomalies for Sb and V, whereas cassiterite from polymetallic vein deposits show a positive anomaly (Wang et al., 2022). Polymetallic vein deposits are generally linked to skarn or greisen deposits occurring in Sn belts. This suggests that the hydrothermal fluids transported Sb and V to polymetallic vein from nearby skarn and or greisen systems, where they were incorporated into cassiterite (e.g., Gemmrich et al., 2021; Liu et al., 2021).

5.4. Discrimination of cassiterite associated with Cu, Zn and Li deposits

Most tin fields contain Cu and Zn mineralization in polymetallic veins and or Li mineralization in LCT pegmatite deposits. Cassiterite grains sourced from these deposits can be discriminated by compositional variation in Zr and Nb. Cassiterite samples from LCT pegmatite deposits are characterized by high concentrations of Nb (avg. 7094 ppm) and Zr (avg. 920 ppm). The chemical boundary differentiating cassiterite sourced from Cu, Zn, and Li deposits was identified through DBSCAN (Fig. 8). Zirconium and Nb have been independently used before to differentiate cassiterite from LCT pegmatite deposits (e.g., Möller and Dulski, 1983; Tindle and Breaks, 1998). The Zr and Nb discrimination plot was evaluated with cassiterite trace element data from Goldmann (2016), and it shows that 86 % of the Li associated cassiterite plot in the Li field (Fig. 9). In fractionated granites, Zr is widely available (Möller and Dulski, 1983; Černý et al., 2005), and is incorporated in cassiterite via direct substitution of Sn (Cheng et al., 2019). The relatively high Nb content in cassiterite from LCT pegmatite deposits are related to high F content and reduced condition (Timofeev et al., 2015). Whereas cassiterite from polymetallic vein deposits with Cu and Zn mineralization are characterized by low Nb and Zr concentrations. Cassiterite trace element data (Goldmann, 2016) for evaluation shows that 95.8 % of the polymetallic Cu-Zn cassiterite plot in the Cu and Zn fields on the Zr and Nb discrimination plot.

5.5. Application of cassiterite discrimination diagrams to placer tin deposits

Cassiterite is resistant to chemical weathering and therefore it can form heavy mineral placer tin deposits (Fig. 10A). The placer cassiterite could be derived from physical weathering of tin deposits including greisen and vein, Sn-skarn, LCT pegmatite, and or polymetallic vein (Fig. 10A). Placer cassiterite trace element data from Goldmann (2016) were plotted on the cassiterite discrimination diagrams (Fig. 10) to examine their association to deposit types and metals. The results obtained from the Al and Ti discrimination diagram showed that placer cassiterite can be successfully linked to tin deposit types (Fig. 10B). While the Zr and Nb discrimination diagram can further predict metal association for these cassiterite deposits (Fig. 10C). The placer cassiterite

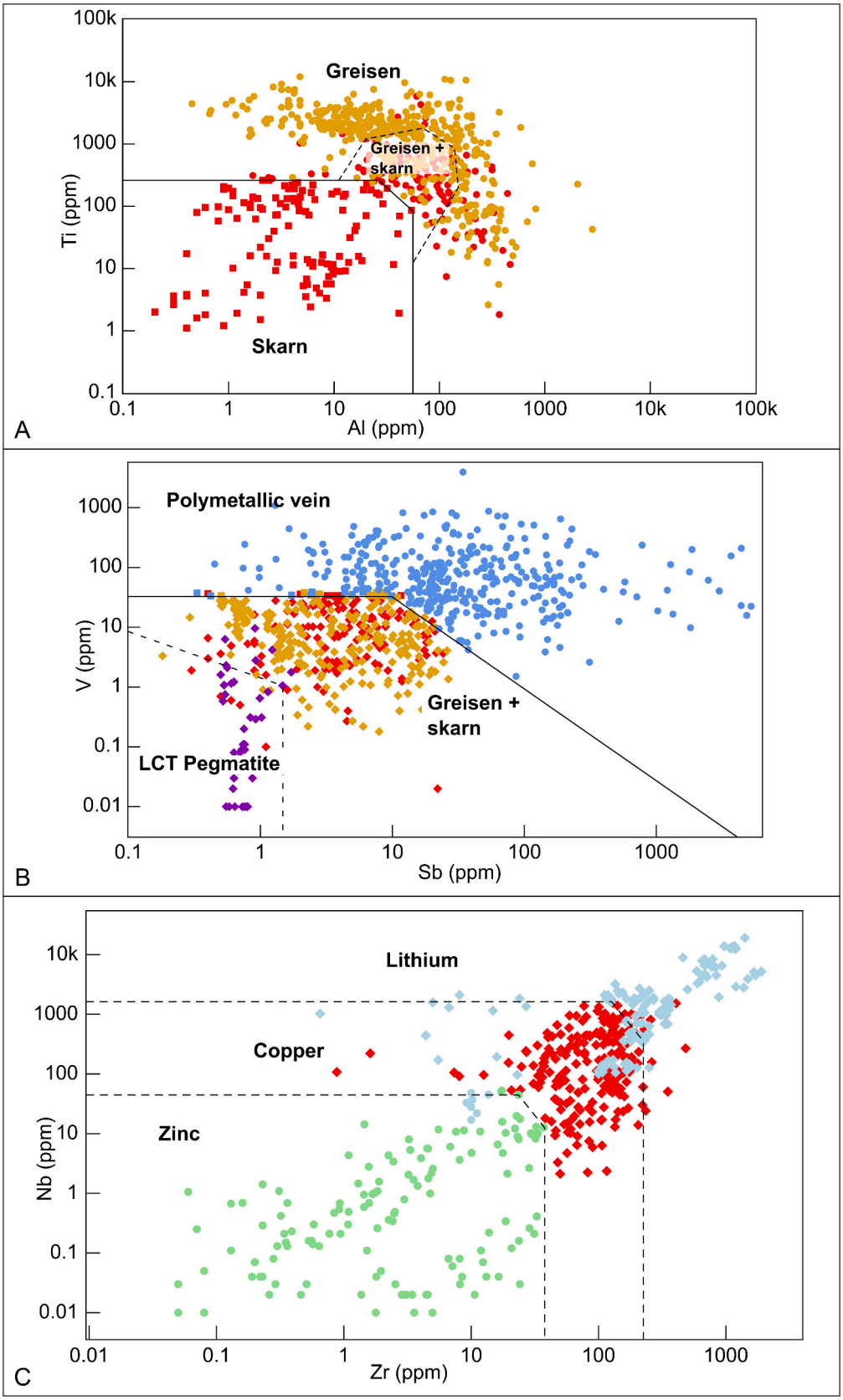

Fig. 8. Cassiterite discrimination plots for: A) skarn, greisen and vein, and skarn composition overlapping with greisen and vein deposits; B) LCT pegmatite and polymetallic vein deposits; C) Li, Cu, and Zn deposits associated with cassiterite.

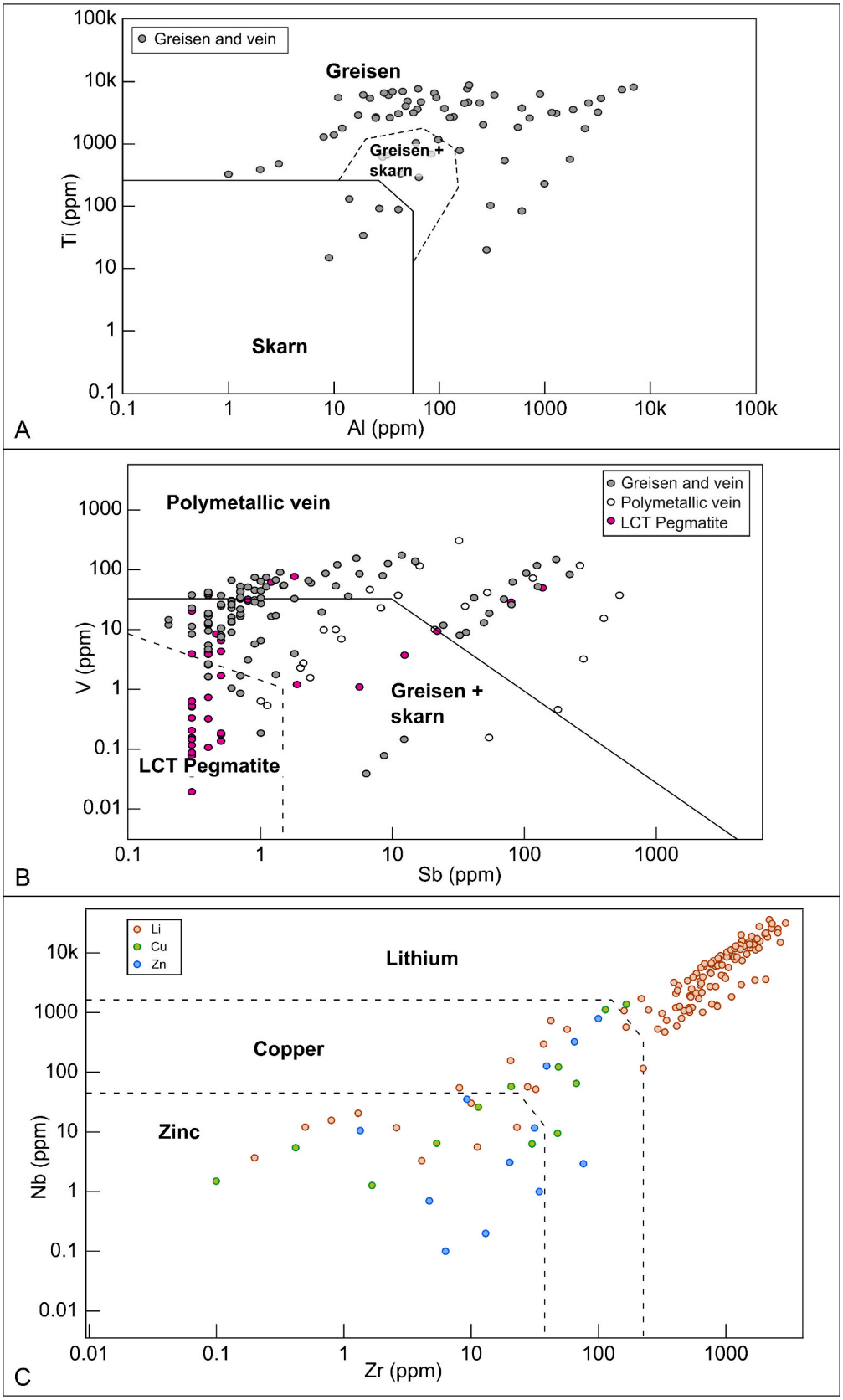

Fig. 9. Cassiterite discrimination diagram with trace element data from Goldmann (2016). A) On the Al vs. Ti discrimination diagram, 92.6 % of the greisen cassiterite plot in the greisen field. B) For the Sb vs. V discrimination diagram, 58.3 % of the polymetallic vein cassiterite plot in the polymetallic vein field, while 53.2 % of the LCT pegmatite cassiterite plot in the pegmatite field. C) On the Zr vs. Nb discrimination diagram, 86 % of the Li associated cassiterite plot in the Li field, and for the polymetallic Cu-Zn sulfide cassiterite, 33.3 % plots in the Cu field and 62.5 % in the Zn field.

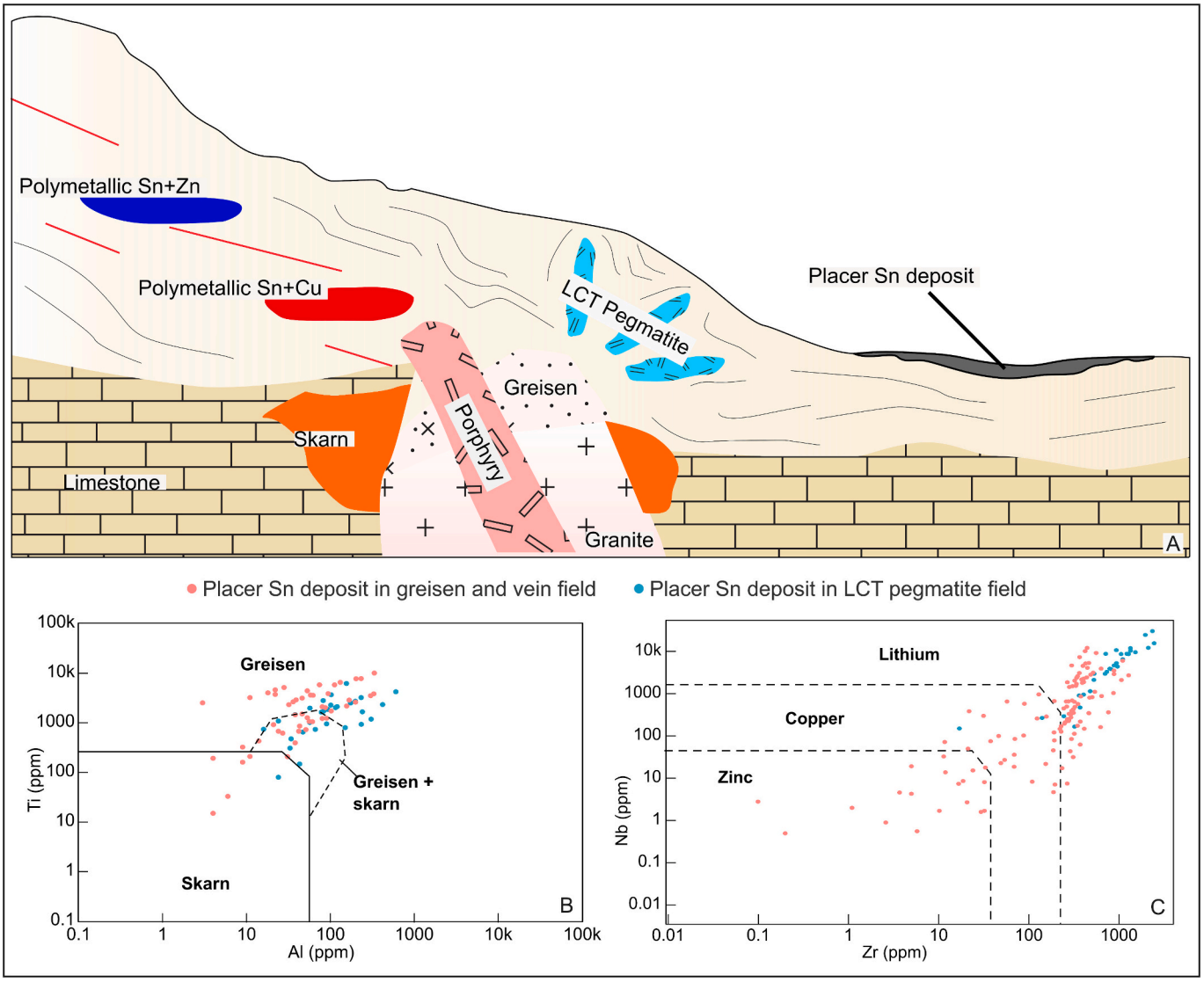

Fig. 10. A) Illustration of placer tin deposit near greisen and vein, skarn, LCT pegmatite, and polymetallic vein deposits. Placer cassiterite trace element data from Goldmann (2016) are plotted on: B) Al and Ti, and C) Zr and Nb discrimination diagrams.

from greisen and vein tin field indicated association with polymetallic Cu and Zn deposits. Since greisen is common in LCT pegmatite, some of these placer deposits are linked to Li deposits (Fig. 10C). Furthermore, placer cassiterite from known LCT pegmatite fields showed accurate association with Li deposits (Fig. 10C). Therefore, these discrimination diagrams can be successfully used in mineral exploration to vector for critical metal deposits with cassiterite samples located from heavy mineral maps (Caritat et al., 2022) and indicator minerals dataset (McClenaghan et al., 2017).

6. Conclusion

Descriptive statistics, correlation matrices, and PCA techniques were used to understand element substitution in cassiterite grains from different tin deposits occurring in seven major tin fields. These tin field include the Andean Sn belt in South America; the Karagwe Ankole belt in Rwanda; the HMF in Australia; and the Kangxiwa-Dahongliutan pegmatite field, Youjiang basin, Nanling belt, and Da Hinggan Range belt in China. The results indicate that Fe substitution in cassiterite is common in greisen and vein, V and Nb substitution in polymetallic vein, Fe and Ti substitution in skarn, and Al and Ga substitution in LCT pegmatite deposits. The DBSCAN method was used to classify cassiterite from different cassiterite-bearing deposits based on trace element distribution patterns. The element pair, Al and Ti can be used to discriminate between greisen and vein, and skarn tin deposits. On this plot, the polymetallic vein and LCT pegmatite data of cassiterite shows compositional overlapping with greisen and vein fields. The discriminant diagram derived from Sb and V can be used to differentiate cassiterite from polymetallic vein deposits. Cassiterite grains linked to Li, Cu and Zn deposits can be differentiated with Nb and Zr discrimination diagram. The discrimination diagrams developed in this study can be used to explore for Cu, Zn, and Li deposits in tin fields with detrital cassiterite from stream sediments, till and heavy mineral placer deposits.

CRediT authorship contribution statement

Avish A. Kumar: Writing – original draft. **Ioan V. Sanislav:** Writing – review & editing, Supervision, Funding acquisition. **Huiqing Huang:** Methodology, Data curation. **Paul H.G.M. Dirks:** Writing – review & editing.

Declaration of competing interest

The authors declare that they have no known competing financial interests or personal relationships that could have appeared to influence the work reported in this paper.

Data availability

Original cassiterite trace element data is included in the supplementary file.

Acknowledgements

This research was funded by the Geological Survey of Queensland under the New Economy Minerals Initiative (NEMI), and AAK was supported by a Commonwealth Research scholarship at James Cook University. We thank the Economic Geology Research Centre (EGRU) at James Cook University, Townsville, Australia for supporting us in successfully conducting this research.

Appendix A. Supplementary data

Supplementary data to this article can be found online at https://doi.org/10.1016/j.gexplo.2024.107530.

References

Abdelnasser, A., Kumral, M., Zoheir, B., Yilmaz, H., 2022. Evolution of the Tepeoba porphyry-skarn Cu-Mo-Au deposit, NW Turkey: new mineralogical and geochemical findings. Ore Geol. Rev. 147, 104967 https://doi.org/10.1016/j.oregeorev.2022.104967.

Aitchison, J., 1982. The statistical analysis of compositional data. J. R. Stat. Soc. B. Methodol. 44, 139–160. https://doi.org/10.1111/j.2517-6161.1982.tb01195.x.

Aitchison, J., Barceló-Vidal, C., Martín-Fernández, J.A., Pawlowsky-Glahn, V., 2000. Logratio analysis and compositional distance. Math. Geol. https://doi.org/10.1023/A:1007529726302.

Alekseev, V.I., Marin, Yu.B., 2022. Accessory cassiterite as an indicator of rare metal petrogenesis and mineralization. Geol. Ore Deposits 64, 397–423. https://doi.org/10.1134/S1075701522070029.

Aleva, G.J.J., 1985. Indonesian fluvial cassiterite placers and their genetic environment. J. Geol. Soc. Lond. 142, 815–836. https://doi.org/10.1144/gsjgs.142.5.0815.

Andersen, J.C.Ø., Stickland, R.J., Rollinson, G.K., Shail, R.K., 2016. Indium mineralisation in SW England: host parageneses and mineralogical relations. Ore Geol. Rev. 78, 213–238. https://doi.org/10.1016/j.oregeorev.2016.02.019.

Atkinson, A.C., Riani, M., Corbellini, A., 2021. The Box–Cox transformation: review and extensions. Stat. Sci. 36 https://doi.org/10.1214/20-STS778.

Audétat, A., Günther, D., Heinrich, C.A., 2000. Causes for large-scale metal zonation around mineralized plutons: fluid inclusion LA-ICP-MS evidence from the Mole Granite, Australia. Econ. Geol. 95, 1563–1581. https://doi.org/10.2113/gsecongeo.95.8.1563.

Auwera, V.J., Andre, L., 1991. Trace elements (REE) and isotopes (O, C, Sr) to characterize the metasomatic fluid sources: evidence from the skarn deposit (Fe, W, Cu) of Traversella (Ivrea, Italy). Contrib. Mineral. Petrol. 106, 325–339. https://doi.org/10.1007/BF00324561.

Bäcklund, H., Hedblom, A., Neijman, N., 2011. A density-based spatial clustering of application with noise. Data Mining TNM033 33, 11–30.

Benites, D., Torró, L., Vallance, J., Laurent, O., Quispe, P., Rosas, S., Uzieda, M.F., Holm-Denoma, C.S., Pianowski, L.S., Camprubí, A., Colás, V., Fernández-Baca, Á., Giraldo, L., Chelle-Michou, C., Sáez, J., Kouzmanov, K., Fontboté, L., 2022. Geology, mineralogy, and cassiterite geochronology of the Ayawilca Zn-Pb-Ag-In-Sn-Cu deposit, Pasco, Peru. Miner. Depos. 57, 481–507. https://doi.org/10.1007/s00126-021-01066-z.

Bennett, J.M., Kemp, A.I.S., Hagemann, S.G., Fiorentini, M.L., Roberts, M.P., 2024. Systematic trends in the substitution mechanisms of minor elements in cassiterite. Aust. J. Earth Sci. 1–27 https://doi.org/10.1080/08120099.2024.2325396.

Breiter, K., Ďurišová, J., Korbelová, Z., Vašinová Galiová, M., Hložková, M., 2023. Granite pluton at the Panasqueira Tungsten deposit, Portugal: genetic implications as revealed from new geochemical data. Minerals 13, 163. https://doi.org/10.3390/min13020163.

Burt, D.M., 1981. Acidity-salinity diagrams; application to greisen and porphyry deposits. Econ. Geol. 76, 832–843. https://doi.org/10.2113/gsecongeo.76.4.832.

Cacho, A., Melgarejo, J.-C., Camprubí, A., Torró, L., Castillo-Oliver, M., Torres, B., Artiaga, D., Tauler, E., Martínez, Á., Campeny, M., Alfonso, P., Arce-Burgoa, O.R., 2019. Mineralogy and distribution of critical elements in the Sn–W–Pb–Ag–Zn Huanuni deposit, Bolivia. Minerals 9, 753. https://doi.org/10.3390/min9120753.

Caritat, P., McInnes, B., Walker, A., Bastrakov, E., Rowins, S., Prent, A., 2022. The heavy mineral map of Australia: vision and pilot project. Minerals 12, 961. https://doi.org/10.3390/min12080961.

Černý, P., Blevin, P.L., Cuney, M., London, D., 2005. Granite-related ore deposits. In: One Hundredth Anniversary Volume. Society of Economic Geologists, pp. 337–370. https://doi.org/10.5382/AV100.12.

Chen, J., Halls, C., Stanley, C.J., 1992. Tin-bearing skarns of South China: geological setting and mineralogy. Ore Geol. Rev. 7, 225–248. https://doi.org/10.1016/0169-1368(92)90006-7.

Chen, S.-C., Yu, J.-J., Bi, M.-F., Li, H.-M., Lehmann, B., 2022. Cassiterite U–Pb, mica 40Ar–39Ar dating and cassiterite trace-element composition of the Furong tin deposit in the Nanling Range, South China. Ore Geol Rev 143, 104775. https://doi.org/10.1016/j.oregeorev.2022.104775.

Cheng, Y., Mao, J., 2010. Age and geochemistry of granites in Gejiu area, Yunnan province, SW China: constraints on their petrogenesis and tectonic setting. Lithos 120, 258–276. https://doi.org/10.1016/j.lithos.2010.08.013.

Cheng, Y., Mao, J., Chang, Z., Pirajno, F., 2013. The origin of the world class tin-polymetallic deposits in the Gejiu district, SW China: constraints from metal zoning characteristics and 40Ar–39Ar geochronology. Ore Geol. Rev. 53, 50–62. https://doi.org/10.1016/j.oregeorev.2012.12.008.

Cheng, Y., Spandler, C., Chang, Z., Clarke, G., 2018. Volcanic–plutonic connections and metal fertility of highly evolved magma systems: a case study from the Herberton Sn–W–Mo Mineral Field, Queensland, Australia. Earth Planet. Sci. Lett. 486, 84–93. https://doi.org/10.1016/j.epsl.2018.01.012.

Cheng, Y., Spandler, C., Kemp, A., Mao, J., Rusk, B., Hu, Y., Blake, K., 2019. Controls on cassiterite (SnO2) crystallization: evidence from cathodoluminescence, trace-element chemistry, and geochronology at the Gejiu Tin District. Am. Mineral. 104, 118–129. https://doi.org/10.2138/am-2019-6466.

Clarke, G.W., Chang, Z., 2017. Magma-related Hydrothermal Mineral Systems of the Northern Bowen Basin. Unpublished report, Geological Survey of Queensland.

Cook, N.J., Ciobanu, C.L., Pring, A., Skinner, W., Shimizu, M., Danyushevsky, L., Saini-Eidukat, B., Melcher, F., 2009. Trace and minor elements in sphalerite: a LA-ICPMS study. Geochim. Cosmochim. Acta 73, 4761–4791. https://doi.org/10.1016/j.gca.2009.05.045.

Denholm, J.L., Stepanov, A.S., Meffre, S., Bottrill, R.S., Thompson, J.M., 2021. The geochronology of tasmanian tin deposits using LA-ICP-MS U-Pb cassiterite dating. Econ. Geol. 116, 1387–1407. https://doi.org/10.5382/econgeo.4837.

Dewaele, S., Henjes-Kunst, F., Melcher, F., Sitnikova, M., Burgess, R., Gerdes, A., Fernandez, M.A., De Clercq, F., Muchez, P., Lehmann, B., 2011. Late Neoproterozoic overprinting of the cassiterite and columbite-tantalite bearing pegmatites of the Gatumba area, Rwanda (Central Africa). J. Afr. Earth Sci. 61, 10–26. https://doi.org/10.1016/j.jafrearsci.2011.04.004.

Dill, H.G., 2015. Pegmatites and aplites: their genetic and applied ore geology. Ore Geol. Rev. 69, 417–561. https://doi.org/10.1016/j.oregeorev.2015.02.022.

Dmitrijeva, M., Cook, N.J., Ehrig, K., Ciobanu, C.L., Metcalfe, A.V., Kamenetsky, M., Kamenetsky, V.S., Gilbert, S., 2020. Multivariate statistical analysis of trace elements in pyrite: prediction, bias and artefacts in defining mineral signatures. Minerals 10, 61. https://doi.org/10.3390/min10010061.

Dusausoy, Y., Ruck, R., Gaite, J.M., 1988. Study of the symmetry of Fe^{3+} sites in SnO_2 by electron paramagnetic resonance. Phys. Chem. Miner. 15, 300–303. https://doi.org/10.1007/BF00307520.

Ester, M., Kriegel, H.-P., Sander, J., Xu, X., 1996. A density-based algorithm for discovering clusters in large spatial databases with noise. In: KDD-96 Proc, pp. 226–231.

Feng, Y., Liang, T., Yang, X., Zhang, Z., Wang, Y., 2019. Chemical evolution of Nb-Ta oxides and cassiterite in phosphorus-rich albite-spodumene pegmatites in the Kangxiwa–Dahongliutan Pegmatite Field, Western Kunlun Orogen, China. Minerals 9, 166. https://doi.org/10.3390/min9030166.

Fontboté, L., 2018. Ore deposits of the Central Andes. Elements 14, 257–261. https://doi.org/10.2138/gselements.14.4.257.

Frenzel, M., 2023. Making sense of mineral trace-element data – how to avoid common pitfalls in statistical analysis and interpretation. Ore Geol. Rev. https://doi.org/10.1016/j.oregeorev.2023.105566.

Ge, Y.-Z., Zhang, Z.-J., Cheng, Q.-M., Wu, G.-P., 2022. Geological mapping of basalt using stream sediment geochemical data: Case study of covered areas in Jining, Inner Mongolia, China. J. Geochem. Explor. 232, 106888 https://doi.org/10.1016/j.gexplo.2021.106888.

Gemmrich, L., Torró, L., Melgarejo, J.C., Laurent, O., Vallance, J., Chelle-Michou, C., Sempere, T.P.A., 2021. Trace element composition and U-Pb ages of cassiterite from the Bolivian tin belt. Miner. Depos. 56, 1491–1520. https://doi.org/10.1007/s00126-020-01030-3.

Goldmann, S., 2016. Mineralogical-geochemical Characterisation of Cassiterite and Wolframite Ores for an Analytical Fingerprint: Focus on Trace Element Analysis by LA-ICP-MS. PhD thesis.. Leibniz University Hannover, Germany.

Greaves, G., Stevenson, B.G., Taylor, R.G., 1971. Magnetic cassiterites from Herberton, north Queensland, Australia. Econ. Geol. 66, 480–487. https://doi.org/10.2113/gsecongeo.66.3.480.

Halley, S.W., Walshe, J.L., 1995. A reexamination of the Mount Bischoff cassiterite sulfide skarn, western Tasmania. Econ. Geol. 90, 1676–1693. https://doi.org/10.2113/gsecongeo.90.6.1676.

Halter, W.E., Williams-Jones, A.E., Kontak, D.J., 1996. The role of greisenization in cassiterite precipitation at the East Kemptville tin deposit, Nova Scotia. Econ. Geol. 91, 368–385. https://doi.org/10.2113/gsecongeo.91.2.368.

Hao, J., Ho, T.K., 2019. Machine learning made Easy: a review of scikit-learn package in python programming language. J. Educ. Behav. Stat. 44, 348–361. https://doi.org/10.3102/1076998619832248.

He, X., Bao, C., Lu, Y., Leonard, N., Liu, Z., Tan, S., 2022a. LA–ICP–MS U–Pb dating, elemental mapping and in situ trace element analyses of cassiterites from the gejiu tin polymetallic deposit, SW China: constraints on the timing of mineralization and

precipitation environment. Minerals 12, 313. https://doi.org/10.3390/min12030313.
He, X., Zhao, J., Zhou, R., Feng, Y., Leonard, N., Li, F., Liu, Z., Li, W., Tan, S., 2022b. The distribution and substitution mechanism of trace elements in cassiterites: constraints from LA-ICP-MS U–Pb dating, elemental mapping and in situ trace element analyses of the Gejiu tin polymetallic deposit, SW China. Chem. Geol. 609 https://doi.org/10.1016/j.chemgeo.2022.121063.
Hong, J., Oh, S., 2021. Model selection for mineral resource assessment considering geological and grade uncertainties: application of multiple-point geostatistics and a cluster analysis to an iron deposit. Nat. Resour. Res. 30, 2047–2065. https://doi.org/10.1007/s11053-021-09813-9.
Hreus, S., Výravský, J., Cempírek, J., Breiter, K., Vašinová Galiová, M., Krátký, O., Šešulka, V., Škoda, R., 2021. Scandium distribution in the world-class Li-Sn-W Cínovec greisen-type deposit: result of a complex magmatic to hydrothermal evolution, implications for scandium valorization. Ore Geol. Rev. 139, 104433 https://doi.org/10.1016/j.oregeorev.2021.104433.
Huang, H.-Q., Guillong, M., Hu, Y., Spandler, C., 2021. Fine tuning laser focus for improved reproducibility of U–Pb isotope analysis by LA-ICP-MS. J. Anal. At. Spectrom 36, 836–844. https://doi.org/10.1039/D1JA00044F.
Izenman, Alan Julian, 2013. Linear dimensionality reduction. In: Izenman, Alan J. (Ed.), Modern Multivariate Statistical Techniques: Regression, Classification, and Manifold Learning. Springer, New York, New York, NY, pp. 195–236. https://doi.org/10.1007/978-0-387-78189-1_7.
Izoret, L., Marnier, G., Dusausoy, Y., 1985. Caracterisation cristallochimique de la cassiterite des gisements d'etain et de tungstene de Galice, Espagne. Can. Mineral. 23, 221–231.
Jansson, N.F., Allen, R.L., Skogsmo, G., Tavakoli, S., 2022. Principal component analysis and K-means clustering as tools during exploration for Zn skarn deposits and industrial carbonates, Sala area, Sweden. J. Geochem. Explor. 233, 106909 https://doi.org/10.1016/j.gexplo.2021.106909.
Jolly, K., 2018. Machine Learning with Scikit-learn Quick Start Guide: Classification, Regression, and Clustering Techniques in Python. Packt Publishing Ltd.
Kelly, W.C., Turneaure, F.S., 1970. Mineralogy, paragenesis and geothermometry of the tin and tungsten deposits of the eastern Andes, Bolivia. Econ. Geol. 65, 609–680. https://doi.org/10.2113/gsecongeo.65.6.609.
Kendall-Langley, L.A., Kemp, A.I.S., Grigson, J.L., Hammerli, J., 2020. U-Pb and reconnaissance Lu-Hf isotope analysis of cassiterite and columbite group minerals from Archean Li-Cs-Ta type pegmatites of Western Australia. Lithos 352–353, 105231. https://doi.org/10.1016/j.lithos.2019.105231.
Konopelko, D.L., Cherny, R.I., Petrov, S.V., Strekopytov, S., Seltmann, R., Vlasenko, N.S., Strekopytov, V.V., Mamadjanov, Y.M., Wang, X.-S., Plotinskaya, O.Yu., Andreeva, E. M., 2022. The Mushiston Sn deposit in Tajik Tien Shan as the type locality for stannite-cassiterite-hydrostannate mineralization: New mineral chemistry data and genetic constraints. J. Geochem. Explor. 239, 107017 https://doi.org/10.1016/j.gexplo.2022.107017.
Konzett, J., Hauzenberger, C., Ludwig, T., Stalder, R., 2018. Anatectic granitic pegmatites from the Eastern Alps: a case of variable rare metal enrichment during high-grade regional metamorphism. II: pegmatite staurolite as an indicator of anatectic pegmatite parent melt formation – a field and experimental study. Can. Mineral. 56, 603–624. https://doi.org/10.3749/canmin.1800011.
Kumar, A.A., Sanislav, I.V., Dirks, P.H.G.M., 2022. The geological setting of the indium-rich Baal Gammon and Isabel Sn-Cu-Zn deposits in the Herberton Mineral Field, Queensland, Australia. Ore Geol. Rev. 149, 105095 https://doi.org/10.1016/j.oregeorev.2022.105095.
Kumar, A., Sanislav, I., Martin, L., et al., 2023a. Genesis of copper mineralization in the polymetallic tin deposits from the Herberton Mineral Field, Queensland, Australia. Miner. Depos. https://doi.org/10.1007/s00126-023-01209-4.
Kumar, A.A., Sanislav, I.V., Cathey, H.E., Dirks, P.H.G.M., 2023b. Geochemistry of indium in magmatic-hydrothermal tin and sulfide deposits of the Herberton Mineral Field, Australia. Miner Depos. https://doi.org/10.1007/s00126-023-01179-7.
Launay, G., Branquet, Y., Sizaret, S., Guillou-Frottier, L., Gloaguen, E., 2023. How greisenization could trigger the formation of large vein-and-greisen Sn-W deposits: a numerical investigation applied to the Panasqueira deposit. Ore Geol. Rev. 153, 105299 https://doi.org/10.1016/j.oregeorev.2023.105299.
Layne, G.D., Spooner, E.T.C., 1991. The JC tin skarn deposit, southern Yukon Territory; I, Geology, paragenesis, and fluid inclusion microthermometry. Econ. Geol. 86, 29–47. https://doi.org/10.2113/gsecongeo.86.1.29.
Lehmann, B., 1990. Metallogeny of Tin, Lecture Notes in Earth Sciences. Springer-Verlag, Berlin/Heidelberg. https://doi.org/10.1007/BFb0010922.
Lehmann, B., 2021. Formation of tin ore deposits: a reassessment. Lithos 402–403, 105756. https://doi.org/10.1016/j.lithos.2020.105756.
Li, Z.X., Li, X.H., Chung, S.L., Lo, C.H., Xu, X., Li, W.X., 2012. Magmatic switch-on and switch-off along the South China continental margin since the Permian: transition from an Andean-type to a Western Pacific-type plate boundary. Tectonophysics 532–535, 271–290. https://doi.org/10.1016/j.tecto.2012.02.011.
Li, H., Palinkaš, L.A., Watanabe, K., Xi, X.-S., 2018. Petrogenesis of Jurassic A-type granites associated with Cu-Mo and W-Sn deposits in the central Nanling region, South China: relation to mantle upwelling and intra-continental extension. Ore Geol. Rev. 92, 449–462. https://doi.org/10.1016/j.oregeorev.2017.11.029.
Li, Y., Liu, Z., Shao, Y., Chen, K., Zhang, J., Zhang, Y., Zhang, T., 2022a. Genesis of the Huangangliang Fe-Sn polymetallic deposit in the southern Da Hinggan Range, NE China: constraints from geochronology and cassiterite trace element geochemistry. Ore Geol. Rev. 151, 105226 https://doi.org/10.1016/j.oregeorev.2022.105226.
Li, Y., Zhang, R., Ji, H., Wang, C., Tan, J., Wei, J., 2022b. Chemistry and U–Pb geochronology of cassiterite in the Xiasai deposit, central Yidun Terrane (SW China): link between Sn and Ag–Pb–Zn mineralisation. Ore Geol. Rev. 149, 105106 https://doi.org/10.1016/j.oregeorev.2022.105106.
Liu, Z., Jiang, Y.H., Jia, R.Y., Zhao, P., Zhou, Q., 2015. Origin of Late Triassic high-K calc-alkaline granitoids and their potassic microgranular enclaves from the western Tibet Plateau, northwest China: Implications for Paleo-Tethys evolution. Gondw. Res. 27, 326–341. https://doi.org/10.1016/j.gr.2013.09.022.
Liu, S., Liu, Y., Ye, L., Wei, C., Cai, Y., Chen, W., 2021. Genesis of dulong Sn-Zn-In polymetallic deposit in Yunnan Province, South China: insights from cassiterite U-Pb ages and trace element compositions. Minerals 11, 199. https://doi.org/10.3390/min11020199.
London, D., 2014. A petrologic assessment of internal zonation in granitic pegmatites. Lithos 184–187, 74–104. https://doi.org/10.1016/j.lithos.2013.10.025.
London, D., 2018. Ore-forming processes within granitic pegmatites. Ore Geol. Rev. 101, 349–383. https://doi.org/10.1016/j.oregeorev.2018.04.020.
Maldener, J., Rauch, F., Gavranic, M., Beran, A., 2001. OH absorption coefficients of rutile and cassiterite deduced from nuclear reaction analysis and FTIR spectroscopy. Mineral. Petrol. 71, 21–29. https://doi.org/10.1007/s007100170043.
Mao, J., Li, H., Shimazaki, H., Raimbault, L., Guy, B., 1996. Geology and metallogeny of the Shizhuyuan Skarn-Greisen deposit, Hunan Province, China. Int. Geol. Rev. 38, 1020–1039. https://doi.org/10.1080/00206819709465379.
Mao, J., Cheng, Y., Chen, M., Pirajno, F., 2013. Major types and time–space distribution of Mesozoic ore deposits in South China and their geodynamic settings. Miner. Depos. 48, 267–294. https://doi.org/10.1007/s00126-012-0446-z.
Mao, J., Zheng, W., Xie, G., Lehmann, B., Goldfarb, R., 2021. Recognition of a Middle–Late Jurassic arc-related porphyry copper belt along the southeast China coast: geological characteristics and metallogenic implications. Geology 49, 592–596. https://doi.org/10.1130/G48615.1.
Masau, M., Černý, P., Chapman, R., 2000. Exsolution of zirconian-hafnian wodginite Annie claim #3 granitic pegmatite, Southeastern Manitoba, Canada. Can. Mineral. 38, 685–694. https://doi.org/10.2113/gscanmin.38.3.685.
McClenaghan, M.B., Parkhill, M.A., Pronk, A.G., Sinclair, W.D., 2017. Indicator mineral and till geochemical signatures of the Mount Pleasant W-Mo-Bi and Sn-Zn-In deposits, New Brunswick, Canada. J. Geochem. Explor. 172, 151–166. https://doi.org/10.1016/j.gexplo.2016.10.004.
Meinert, L.D., 1992. Skarns and Skarn Deposits. Geosci. Can. 19.
Melnykov, V., Wang, Y., 2023. Conditional mixture modeling and model-based clustering. Pattern Recognit. 133, 108994 https://doi.org/10.1016/j.patcog.2022.108994.
Meng, X., Zhang, D., Zhang, R., Wang, J., Zhang, F., Yu, Z., Noel, W.C., Zhou, T., 2022. Geochronology and geochemical characteristics of ore-forming granite in Maopengdian Sn deposit, northern Jiangxi Province. Ore Geol. Rev. 149, 105098 https://doi.org/10.1016/j.oregeorev.2022.105098.
Mlynarczyk, M.S.J., Williams-Jones, A.E., 2005. The role of collisional tectonics in the metallogeny of the Central Andean tin belt. Earth Planet. Sci. Lett. 240, 656–667. https://doi.org/10.1016/j.epsl.2005.09.047.
Möller, P., Dulski, P., 1983. Fractionation of Zr and Hf in cassiterite. Chem. Geol. 40, 1–12. https://doi.org/10.1016/0009-2541(83)90087-6.
Möller, P., Dulski, P., Szacki, W., Malow, G., Riedel, E., 1988. Substitution of tin in cassiterite by tantalum, niobium, tungsten, iron and manganese. Geochim. Cosmochim. Acta 52, 1497–1503. https://doi.org/10.1016/0016-7037(88)90220-7.
Nambaje, C., Eggins, S.M., Yaxley, G.M., Sajeev, K., 2020. Micro-characterisation of cassiterite by geology, texture and zonation: a case study of the Karagwe Ankole Belt, Rwanda. Ore Geol Rev 124, 103609. https://doi.org/10.1016/j.oregeorev.2020.103609.
Nambaje, C., Satish-Kumar, M., Williams, I.S., Takahashi, T., Sajeev, K., 2021. Granitic rocks from Rwanda: Vital clues to the tectonic evolution of the Karagwe–Ankole Belt. Lithos 404–405, 106490. https://doi.org/10.1016/j.lithos.2021.106490.
Neiva, A.M.R., 1996. Geochemistry of cassiterite and its inclusions and exsolution products from tin and tungsten deposits in Portugal. Canadian Mineralo gist 34, 745–768.
Neiva, A.M.R., 2008. Geochemistry of cassiterite and wolframite from tin and tungsten quartz veins in Portugal. Ore Geol. Rev. 33, 221–238. https://doi.org/10.1016/j.oregeorev.2006.05.013.
Niu, X., Shu, Q., Xing, K., Yuan, S., Wei, L., Zhang, Y., Yu, F., Zeng, Q., Ma, S., 2022. Evaluating Sn mineralization potential at the Haobugao skarn Zn–Pb deposit (NE China) using whole-rock and zircon geochemistry. J. Geochem. Explor. 234, 106938 https://doi.org/10.1016/j.gexplo.2021.106938.
Nwamba, M.N., Kelepile, T., Ngatcha, R.B., Suh, C.E., Ilouga, C.D.I., Shemang, E.M., Tantoh, B.S., Tata, E., Agyingi, C.M., 2023. Compositional provenance study of alluvial cassiterite at Bambol and Mayo Seni localities of the Mayo Darlé massif, northern Cameroon. J. Sed. Environ. https://doi.org/10.1007/s43217-023-00136-8.
Olivier, J., Norberg, M.M., 2010. Positively Skewed data: revisiting the Box-Cox power transformation. Int. J. Psychol. Res. (Medellin) 3, 69–78.
Pal, D.C., Mishra, B., Bernhardt, H.-J., 2007. Mineralogy and geochemistry of pegmatite-hosted Sn-, Ta–Nb-, and Zr–Hf-bearing minerals from the southeastern part of the Bastar-Malkangiri pegmatite belt, Central India. Ore Geol. Rev. 30, 30–55. https://doi.org/10.1016/j.oregeorev.2005.10.004.
Paton, C., Hellstrom, J., Paul, B., Woodhead, J., Hergt, J., 2011. Iolite: freeware for the visualisation and processing of mass spectrometric data. J. Anal. At. Spectrom 26, 2508. https://doi.org/10.1039/c1ja10172b.
Pedregosa, F., Varoquaux, G., Gramfort, A., Michel, V., Thirion, B., Grisel, O., Blondel, M., Prettenhofer, P., Weiss, R., Dubourg, V., 2011. Scikit-learn: machine learning in Python. J. Mach. Learn. Res. 12, 2825–2830.
Poblete, J.A., Dirks, P.H.G.M., Chang, Z., Huizenga, J.M., Griessmann, M., Hall, C., 2021. The watershed tungsten deposit, Northeast Queensland, Australia: permian

metamorphic tungsten mineralization overprinting carboniferous magmatic tungsten. Econ. Geol. 116, 427–451. https://doi.org/10.5382/econgeo.4791.
Roberts, D.E., 2007. Metasomatism and the formation of greisen in Grainsgill, Cumbria, England. Geol. J. 18, 43–52. https://doi.org/10.1002/gj.3350180104.
Romer, R.L., Kroner, U., 2016. Phanerozoic tin and tungsten mineralization—Tectonic controls on the distribution of enriched protoliths and heat sources for crustal melting. Gondw. Res. 31, 60–95. https://doi.org/10.1016/j.gr.2015.11.002.
Scealy, J.L., Welsh, A.H., 2014. Colours and cocktails: compositional data analysis 2013 Lancaster lecture. Aust. N. Z. J. Stat. 56, 145–169. https://doi.org/10.1111/anzs.12073.
Schubert, E., Sander, J., Ester, M., Kriegel, H.P., Xu, X., 2017. DBSCAN revisited, revisited: why and how you should (still) use DBSCAN. ACM Trans. Database Syst. 42 https://doi.org/10.1145/3068335.
Selway, J.B., Breaks, F.W., Tindle, A.G., 2005. A review of rare-element (Li-Cs-Ta) pegmatite exploration techniques for the superior Province, Canada, and large worldwide tantalum deposits. Explor. Min. Geol. 14, 1–30. https://doi.org/10.2113/gseng.14.1-4.1.
Sempere, T., 1995. Phanerozoic evolution of Bolivia and adjacent regions. In: Petroleum Basins of South America. American Association of Petroleum Geologists. https://doi.org/10.1306/M62593C9.
Sempere, T., Carlier, G., Soler, P., Fornari, M., Carlotto, V., Jacay, J., Arispe, O., Néraudeau, D., Cárdenas, J., Rosas, S., Jiménez, N., 2002. Late Permian–Middle Jurassic lithospheric thinning in Peru and Bolivia, and its bearing on Andean-age tectonics. Tectonophysics 345, 153–181. https://doi.org/10.1016/S0040-1951(01)00211-6.
Shu, L., Yao, J., Wang, B., Faure, M., Charvet, J., Chen, Y., 2021. Neoproterozoic plate tectonic process and Phanerozoic geodynamic evolution of the South China Block. Earth Sci. Rev. 216, 103596 https://doi.org/10.1016/j.earscirev.2021.103596.
Sillitoe, R.H., Lehmann, B., 2022. Copper-rich tin deposits. Miner. Depos. 57, 1–11. https://doi.org/10.1007/s00126-021-01078-9.
Simmons, W., Falster, A., Webber, K., Roda-Robles, E., Boudreaux, A.P., Grassi, L.R., Freeman, G., 2016. Bulk Composition of Mt. Mica Pegmatite, Maine, USA: implications for the origin of an Lct type pegmatite by anatexis. Can. Mineral. 54, 1053–1070. https://doi.org/10.3749/canmin.1600017.
Spikings, R., Reitsma, M.J., Boekhout, F., Mišković, A., Ulianov, A., Chiaradia, M., Gerdes, A., Schaltegger, U., 2016. Characterisation of Triassic rifting in Peru and implications for the early disassembly of western Pangaea. Gondw. Res. 35, 124–143. https://doi.org/10.1016/j.gr.2016.02.008.
Steiner, B., 2019. Tools and workflows for grassroots Li–Cs–Ta (LCT) pegmatite exploration. Minerals 9, 499. https://doi.org/10.3390/min9080499.
Taylor, R., Cuff, C., 1979. Geology of Tin Deposits. Elsevier, Amsterdam.
Timofeev, A., Migdisov, Art.A., Williams-Jones, A.E., 2015. An experimental study of the solubility and speciation of niobium in fluoride-bearing aqueous solutions at elevated temperature. Geochim. Cosmochim. Acta 158, 103–111. https://doi.org/10.1016/j.gca.2015.02.015.
Tindle, A., Breaks, F.W., 1998. Oxide minerals of the separation rapids rare-element granitic pegmatite group, Northwestern Ontario. Can. Mineral. 36, 609–635.
Torró, L., Melgarejo, J., Gemmrich, L., Mollinedo, D., Cazorla, M., Martínez, Á., Pujol-Solà, N., Farré-de-Pablo, J., Camprubí, A., Artiaga, D., Torres, B., Alfonso, P., Arce, O., 2019. Spatial and temporal controls on the distribution of indium in xenothermal vein-deposits: the Huari Huari District, Potosí, Bolivia. Minerals 9, 304. https://doi.org/10.3390/min9050304.
Torró, L., Benites, D., Vallance, J., Laurent, O., Ortiz-Benavente, B.A., Chelle-Michou, C., Proenza, J.A., Fontboté, L., 2022. Trace element geochemistry of sphalerite and chalcopyrite in arc-hosted VMS deposits. J. Geochem. Explor. 232, 106882 https://doi.org/10.1016/j.gexplo.2021.106882.
Verhaegen, J., Weltje, G.J., Munsterman, D., 2019. Workflow for analysis of compositional data in sedimentary petrology: provenance changes in sedimentary basins from spatio-temporal variation in heavy-mineral assemblages. Geol. Mag. 156, 1111–1130. https://doi.org/10.1017/S0016756818000584.
Wang, Y., Fan, W., Zhang, G., Zhang, Y., 2013. Phanerozoic tectonics of the South China Block: key observations and controversies. Gondw. Res. 23, 1273–1305. https://doi.org/10.1016/j.gr.2012.02.019.
Wang, C., Zhao, K.-D., Chen, J., Ma, X., 2022. Examining fingerprint trace elements in cassiterite: implications for primary tin deposit exploration. Ore Geol. Rev. 149, 105082 https://doi.org/10.1016/j.oregeorev.2022.105082.
Weltje, G.J., 2012. Quantitative models of sediment generation and provenance: state of the art and future developments. Sediment. Geol. 280, 4–20. https://doi.org/10.1016/j.sedgeo.2012.03.010.
Witt, W.K., 1988. Evolution of high-temperature hydrothermal fluids associated with greisenization and feldspathic alteration of a tin-mineralized granite, northeast Queensland. Econ. Geol. 83, 310–334. https://doi.org/10.2113/gsecongeo.83.2.310.
Wu, F.-Y., Sun, D.-Y., Ge, W.-C., Zhang, Y.-B., Grant, M.L., Wilde, S.A., Jahn, B.-M., 2011. Geochronology of the Phanerozoic granitoids in northeastern China. J. Asian Earth Sci. 41, 1–30. https://doi.org/10.1016/j.jseaes.2010.11.014.
Xu, B., Jiang, S.-Y., Wang, R., Ma, L., Zhao, K., Yan, X., 2015. Late Cretaceous granites from the giant Dulong Sn-polymetallic ore district in Yunnan Province, South China: Geochronology, geochemistry, mineral chemistry and Nd–Hf isotopic compositions. Lithos 218–219, 54–72. https://doi.org/10.1016/j.lithos.2015.01.004.
Yan, Q.-H., Qiu, Z.-W., Wang, H., Wang, M., Wei, X.-P., Li, P., Zhang, R.-Q., Li, C.-Y., Liu, J., 2018. Age of the Dahongliutan rare metal pegmatite deposit, West Kunlun, Xinjiang (NW China): constraints from LA–ICP–MS U–Pb dating of columbite-(Fe) and cassiterite. Ore Geol. Rev. 100, 561–573. https://doi.org/10.1016/j.oregeorev.2016.11.010.
Yang, M.-S., Lai, C.-Y., Lin, C.-Y., 2012. A robust EM clustering algorithm for Gaussian mixture models. Pattern Recogn. 45, 3950–3961. https://doi.org/10.1016/j.patcog.2012.04.031.
Yuan, S., Williams-Jones, A.E., Romer, R.L., Zhao, P., Mao, J., 2019. Protolith-related thermal controls on the decoupling of Sn and W in Sn-W metallogenic provinces: insights from the Nanling Region, China. Econ. Geol. 114, 1005–1012. https://doi.org/10.5382/econgeo.4669.
Zhang, S., Xiao, K., Carranza, E.J.M., Yang, F., Zhao, Z., 2019. Integration of auto-encoder network with density-based spatial clustering for geochemical anomaly detection for mineral exploration. Comput. Geosci. 130, 43–56. https://doi.org/10.1016/j.cageo.2019.05.011.
Zhang, J., Shao, Y., Liu, Z., Chen, K., 2022. Sphalerite as a record of metallogenic information using multivariate statistical analysis: constraints from trace element geochemistry. J. Geochem. Explor. 232, 106883 https://doi.org/10.1016/j.gexplo.2021.106883.
Zhao, K., Jiang, S., Yaohui, J., 2005. Geology and geochemistry of the Furong Tin Deposit, Hunan Province, P.R. China. In: Mineral Deposit Research: Meeting the Global Challenge. Springer, Berlin Heidelberg, Berlin, Heidelberg, pp. 869–871. https://doi.org/10.1007/3-540-27946-6_221.
Zhao, Z., Hou, L., Ding, J., Zhang, Q., Wu, S., 2018. A genetic link between Late Cretaceous granitic magmatism and Sn mineralization in the southwestern South China Block: a case study of the Dulong Sn-dominant polymetallic deposit. Ore Geol. Rev. 93, 268–289. https://doi.org/10.1016/j.oregeorev.2017.12.020.
Zhou, Z.-H., Mao, J.-W., Lyckberg, P., 2012. Geochronology and isotopic geochemistry of the A-type granites from the Huanggang Sn–Fe deposit, southern Great Hinggan Range, NE China: implication for their origin and tectonic setting. J. Asian Earth Sci. 49, 272–286. https://doi.org/10.1016/j.jseaes.2012.01.015.